



HAL
open science

Comparisons between non-interferometric and interferometric passive surface wave imaging methods-towards linear receiver array

Feng Cheng, Jianghai Xia, Zongbo Xu, Jonathan B. Ajo-Franklin

► To cite this version:

Feng Cheng, Jianghai Xia, Zongbo Xu, Jonathan B. Ajo-Franklin. Comparisons between non-interferometric and interferometric passive surface wave imaging methods-towards linear receiver array. *Geophysical Journal International*, 2023, 233, pp.680-699. 10.1093/gji/ggac475 . insu-04155751

HAL Id: insu-04155751

<https://insu.hal.science/insu-04155751>

Submitted on 8 Jul 2023

HAL is a multi-disciplinary open access archive for the deposit and dissemination of scientific research documents, whether they are published or not. The documents may come from teaching and research institutions in France or abroad, or from public or private research centers.

L'archive ouverte pluridisciplinaire **HAL**, est destinée au dépôt et à la diffusion de documents scientifiques de niveau recherche, publiés ou non, émanant des établissements d'enseignement et de recherche français ou étrangers, des laboratoires publics ou privés.

Comparisons between non-interferometric and interferometric passive surface wave imaging methods—towards linear receiver array

Feng Cheng^{1,2}, Jianghai Xia,¹ Zongbo Xu³ and Jonathan B. Ajo-Franklin^{2,4}

¹School of Earth Sciences, Zhejiang University, 38 Zheda Rd., Hangzhou, Zhejiang 310027, China. E-mail: marscfeng@rice.edu

²Department of Earth, Environmental, and Planetary Sciences, Rice University, 6100 Main St., Houston, TX 77005, USA

³Institut de Physique du Globe de Paris, 75205 Paris Cedex 13, France

⁴Lawrence Berkeley National Laboratory, 1 Cyclotron Rd., Berkeley, CA 94720, USA

Accepted 2022 November 29. Received 2022 November 21; in original form 2021 July 20

SUMMARY

Passive seismic methods in highly populated urban areas have gained much attention from the geophysics and civil engineering communities. Linear arrays are usually deployed for passive surface wave investigations because of their high convenience, and passive surface wave imaging methods commonly used for linear arrays can be grouped as non-interferometric methods (e.g. passive multichannel analysis of surface wave, refraction microtremor) and interferometric methods (e.g. multichannel analysis of passive surface waves and spatial autocorrelation). It is well known that the seismic interferometry method is able to retrieve Green's function between inter-station pairs based on passive seismic data and that is how interferometric methods work. Although non-interferometric methods are also popular and effective in near-surface seismic imaging, particularly in the geotechnical industry, there is no theoretical proof to clarify the accuracy and/or the bias of these methods. In this study, we use numerical derivations and simulations to demonstrate the underlying physics for both non-interferometric and interferometric methods, under two common noise source environments including a homogeneous source distribution and a dominant in-line source distribution. We also prove the strength of interferometric methods for accurate dispersion imaging over the non-interferometric methods, and provide a way to estimate the biases in non-interferometric measurements. Finally, we present comprehensive comparisons between different passive surface wave methods with three typical field examples considering various observation systems.

Key words: Seismic interferometry; Seismic noise; Surface waves and free oscillations; Wave propagation.

1 INTRODUCTION

Shear (S)-wave velocity structure can be determined by inverting the dispersive phase velocity of surface waves (Dorman & Ewing 1962), due to the higher sensitivity of dispersion curve to S -wave velocity than other earth properties, like compressional (P)-wave velocity, bulk density and thickness, for a layered earth model (Xia *et al.* 1999). Several methods exist for estimating near-surface S -wave velocity utilizing the dispersion characteristics of surface waves, and they can be classified into two groups related to the energy source type: active surface wave methods and passive surface wave methods. The term 'assive' denotes that the energy sources are not controlled; depending on the frequency band, a wide variety of passive sources can be utilized for surface wave analysis. A commonality of passive techniques is the lack of information on when or where the sources are activated.

The passive surface wave methods use ambient seismic energy from natural or anthropogenic sources (e.g. earthquakes,

ocean-seafloor interaction, traffic and industrial activities). During the past few decades, passive surface wave methods have gained much attentions from both geophysical and civil engineering communities because of the logistical costs and the exploration depth limitations associated with traditional active seismic surveys, especially in highly populated urban areas. Aki (1957) introduced a passive surface wave method to derive the S -wave velocity (V_s) structure by the inversion of spatial autocorrelation (SPAC) curves using microtremor, which is mainly composed of Rayleigh wave energy. Okada & Suto (2003) presented an overview of the SPAC method and further developed a microtremor array measurement (MAM) in order to improve the flexibility of the receiver configuration and explore deeper S -wave velocity structure (Hayashi *et al.* 2016). Chávez-García *et al.* (2006) testified the performance of SPAC method in linear array, and proved the possibility of extending this 2-D method into linear array (Margaryan *et al.* 2009; Kita *et al.* 2011). Louie (2001) presented the refraction microtremor (ReMi) method as a fast and effective passive seismic method based

on the τ - p transformation, or slant-stacking (Thorson & Claerbout 1985). Park *et al.* (2004) introduced a similar strategy for imaging dispersion of passive surface waves using the phase-shift method, or frequency-domain slant-stacking method, called passive multichannel analysis of surface wave (PMASW). Due to their simplicity and effectiveness, these linear array based passive surface wave methods have been widely utilized for basin-scale shear-velocity structure mapping, earthquake hazard class assessment as well as infrastructure seismic site classification (Stephenson *et al.* 2005; Pancha *et al.* 2008, 2017; Louie *et al.* 2011, 2022; Bajaj & Anbazhagan 2019; Asten *et al.* 2022; Hayashi *et al.* 2022).

Seismic interferometry has been used to estimate Green's function between two receivers from the ambient seismic field (Lobkis & Weaver 2001; Campillo & Paul 2003; Shapiro & Campillo 2004; Snieder 2004; Wapenaar 2004; Nakata *et al.* 2014; Fichtner *et al.* 2019, 2020; Paitz *et al.* 2019; Sergeant *et al.* 2020). This approach has been applied to characterize multiple scales of Earth structure: from global scale or continental scale deep-structure imaging in seismology (e.g. Bensen *et al.* 2007; Yang *et al.* 2007; Lin *et al.* 2008; Yao & van der Hilst 2009; Lehujeur *et al.* 2018; Martins *et al.* 2019; Planès *et al.* 2020) to local scale exploration (e.g. Bakulin & Calvert 2006; Wapenaar *et al.* 2008; Draganov *et al.* 2009; Nakata *et al.* 2011; Ali *et al.* 2013; Behm *et al.* 2014; Nakata 2016). In recent years, seismic interferometry has found a variety of applications in the near-surface characterization domain (e.g. Foti *et al.* 2011; O'Connell & Turner 2011; Xu *et al.* 2013; Cheng *et al.* 2015; Foti *et al.* 2017; Cheng *et al.* 2018a, 2021c, b; Behm *et al.* 2019; Castellanos *et al.* 2020). Le Feuvre *et al.* (2015) introduced the use of cross-correlation and beamforming in the passive multichannel analysis of surface waves to enhance coherent signals. Cheng *et al.* (2016) proposed a hybrid method by combining seismic interferometry and multichannel analysis of surface wave (MASW) method to attenuate the potential effects from directional noise sources, called multichannel analysis of passive surface waves (MAPS).

Based on the data processing schemes of the previously mentioned passive surface wave methods, they can be roughly divided into two groups: non-interferometric methods (e.g. ReMi and PMASW) and interferometric methods (e.g. MAPS and SPAC). Fig. 1 provides a general flowchart for non-interferometric and interferometric passive surface wave methods. Non-interferometric methods directly extract dispersion measurements from ambient seismic records (Louie 2001; Park *et al.* 2004), while interferometric methods calculate interferograms before dispersion spectra measurement, where interferograms are either empirical Green's function (Cheng *et al.* 2016; Xu *et al.* 2017) or spatial autocorrelation coefficients, also known as spatially averaged coherency (Asten 2006; Chávez-García *et al.* 2006). Several studies have provided explicit relationships between Green's function (or cross-correlation functions) and spatial autocorrelation results (Asten 2006; Nakahara 2006; Tsai & Moschetti 2010; Haney *et al.* 2012). Interferometric methods appear more reasonable for utilization in passive seismic surveys. Because they retrieve interpretable signals with a specified virtual source (e.g. Green's function or spatially averaged coherency) from ambient seismic records, the process of dispersion analysis is analogous to active source surface wave analysis (e.g. MASW). Recent studies have argued that interferometric methods have advantages over non-interferometric methods (O'Connell & Turner 2011; Le Feuvre *et al.* 2015; Hayashi *et al.* 2015; Cheng *et al.* 2018b). Cheng *et al.* (2016) demonstrated that MAPS would be more accurate than PMASW in the presence of directional ambient source effects. Xu *et al.* (2017) identified how to improve ReMi by combining seismic interferometry and τ - p transform.

There is no theoretical proof to clarify the accuracy and/or the bias of these methods, although they are popular and effective in near-surface seismic imaging, particularly in the geotechnical industry (Pullamannappallil *et al.* 2003; Stephenson *et al.* 2005; Thelen *et al.* 2006; Pancha *et al.* 2008; Park & Miller 2008; Rosenblad & Li 2009; Strobbia & Cassiani 2011; Louie *et al.* 2022). In this study, we use numerical derivations and simulations to improve our understanding of how these methods work, what their strengths are, and how to estimate the biases that exist in surface wave measurements. We first introduce a numerical framework for passive surface wave imaging based on two typical source distribution models, random and linear distribution models. We derive approximate solutions for both non-interferometric and interferometric passive surface wave methods within this framework, and present a way to estimate the bias of non-interferometric imaging method using array smoothing functions. Next, we show three field examples to make further comparisons between different passive surface wave methods. Finally, we summarize the advantages and disadvantages for both non-interferometric and interferometric passive surface wave methods.

We should note that this work focuses on the linear receiver array, which is often deployed for passive surface-wave investigations because of its high efficiency and convenience. In populated urban areas, it is challenging to construct dense 2-D arrays due to the spatial restrictions imposed by existing infrastructure (Liu *et al.* 2020). Linear receiver arrays are a natural geometry for road-side investigations utilizing receivers deployed on shoulders or median strip areas. Therefore, SPAC method discussed in this work is also the linear-array based SPAC method (Chávez-García *et al.* 2006; Margaryan *et al.* 2009; Kita *et al.* 2011), rather than the traditional SPAC (Aki 1957) using a circle array or the two-station SPAC (Ekström *et al.* 2009; Hayashi *et al.* 2013), although they all share the same mathematical base of fitting the Bessel function (the function itself or the zero-crossing of the function) with the spatial autocorrelation coefficient; under the considering of 2-D array, for example dense nodal array, SPAC method is flexible for various geometry configurations (Asten & Hayashi 2018; Cho & Iwata 2021) and can be extended to multicomponent recordings (Haney *et al.* 2012). With increasing attentions paid on the powerful train sources, linear arrays will definitely contribute to shallow structure seismic imaging and monitoring (Quiros *et al.* 2016; Fuchs & Bokelmann 2018; Cheng *et al.* 2019; Liu *et al.* 2021; Yan *et al.* 2021). Linear array techniques are also useful when processing distributed acoustic sensing (DAS) data sets, a recently developed technique which utilizes subsurface fibre-optic to capture earth vibrations for seismic imaging (Dou *et al.* 2017; Ajo-Franklin *et al.* 2019; Zhan 2020; Cheng *et al.* 2021a, 2022). However, attentions should also be paid to the limitations (or inaccuracy) of the linear array configuration in terms of handling irregular ambient noise source distributions (Cheng *et al.* 2016, 2017; Foti *et al.* 2017; Liu *et al.* 2020). Highly directional ambient sources are not considered in this work; under such case, all of above mentioned linear array-based passive surface wave methods require additional azimuthal adjustment to avoid apparent velocity overestimation (Le Feuvre *et al.* 2015; Cheng *et al.* 2016). One possible solution is the use of 2-D adaptive arrays, for example, T-shape, L-shape or crossing-shape arrays along roadways of interest, for better azimuthal averaging (Foti *et al.* 2014; Darvasi 2021; Morton *et al.* 2021); another solution is the use of irregular 2-D arrays combined with the specific algorithms, like krSPAC (Stephenson *et al.* 2019). We should also clarify that the ReMi method discussed in this study does not base its estimates on the subjectively picking the lower borders of the dispersion energy

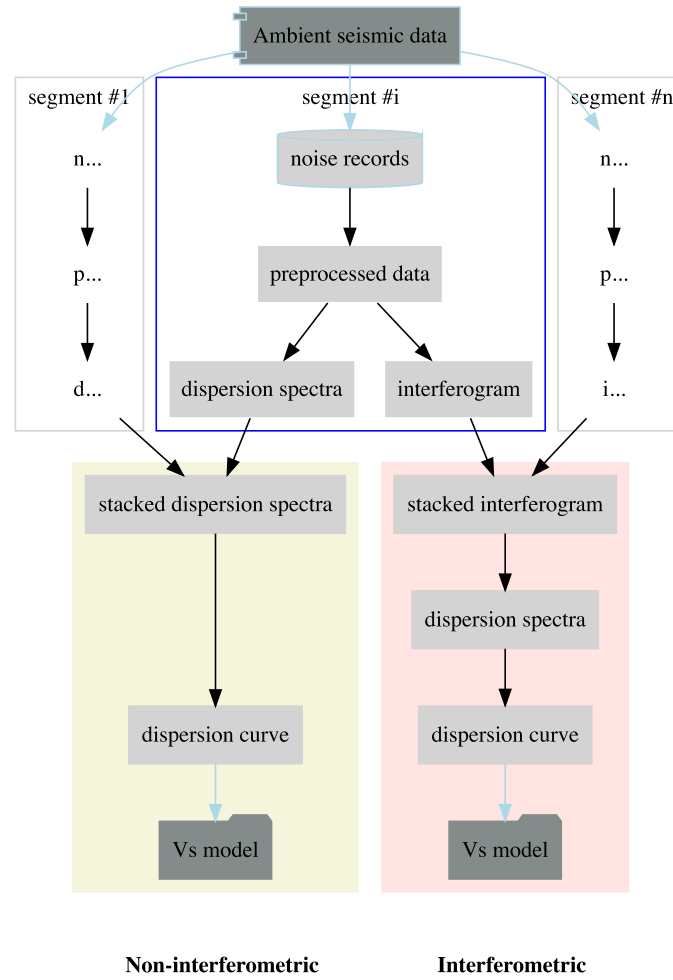


Figure 1. Flowchart for two types of passive surface wave methods, non-interferometric and interferometric approaches.

as suggested by Louie (2001) and Louie *et al.* (2022) but on the objectively defined energy peaks, considering the poor definition of the ‘lower’ contours which depend on the subjectively chosen colour map (Mulargia & Castellaro 2013).

2 A NUMERICAL FRAMEWORK FOR PASSIVE SURFACE WAVE IMAGING

In order to provide a quantitative understanding of the different imaging techniques, we use a numerical framework to derive the various imaging schemes for these passive surface wave methods, including PMASW, ReMi, MAPS and SPAC. For a stratified medium, the contribution of the time–space unrelated ambient noise sources to a seismogram can be written as (Aki & Richards 2002; Lawrence *et al.* 2013; Cheng *et al.* 2016):

$$u(x, \omega) = \sum_{i=1}^{N_s} F(s_i, \omega) e^{j(\omega t_{s_i} - k_0(\omega) r_{s_i x}) - \alpha(\omega) r_{s_i x}} / \sqrt{r_{s_i x}}, \quad (1)$$

where $u(x, \omega)$ is the vertical component of displacement of the noise wavefield obtained at receiver x (here we consider the even-sampled linear array case, where the interstation distance is defined as dx), $F(s_i, \omega)$ denotes the spectrum of a single point-force source located at s_i , ω is the angular frequency, j is the unit imaginary number, N_s is the total source number, $k_0(\omega)$ is the fundamental mode surface wave

wavenumber (multiple modes are not considered in this derivation), t_{s_i} is the source emitting time, $\alpha(\omega)$ is the frequency-dependent attenuation coefficient, $r_{s_i x}$ is the source–receiver distance. $\sqrt{r_{s_i x}}$, the geometric (cylindrical) damping term, is neglected in this work since it is an amplitude-modulation factor, which will be generally cancelled by the spectral whitening operator during the ambient seismic data pre-processing. For convenience, we use the general assumptions, which have been involved in mathematical derivations of many passive seismic methods. In the context of this work, we list them here:

1. The far-field approximation ($r_{s_i x} \gg dx$; Tromp & Dahlen 1993; Nishida 2011; Lawrence *et al.* 2013).
 2. The lossless medium assumption ($\alpha \approx 0$; Wapenaar 2004; Wapenaar & Ruigrok 2011; Draganov *et al.* 2013).
 3. The white-source field assumption ($F(s_i, \omega) \approx \overline{F(\omega)} = 1$; Lobkis & Weaver 2001; Kimman & Trampert 2010; Lawrence *et al.* 2013).
- Fig. 2 illustrates the geometric relationship between the receiver X and the source S_i under the far-field approximation,

$$\begin{aligned} r_{s_i x} &\approx r_{s_i} + x \cos \varphi_i \\ &\approx r_{s_i} + x \cos \theta_i, \end{aligned} \quad (2)$$

where θ_i is the azimuth of source S_i ; φ_i is the azimuth between receiver X and source S_i . θ_i is approximate to φ_i , and varies from 0 to 2π .

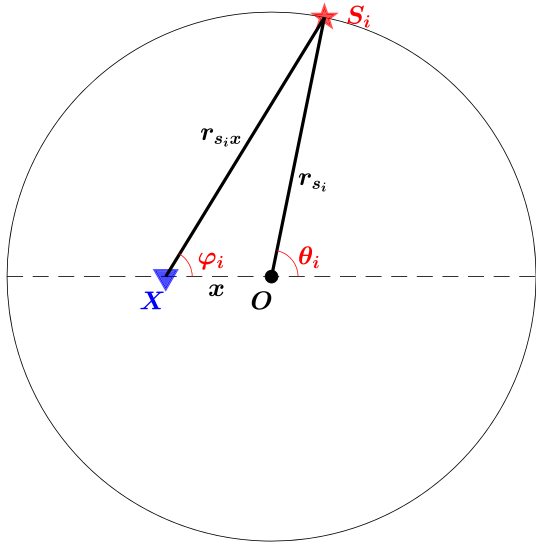


Figure 2. Geometric description of the far-field approximation in eq (2). The variables include source location s_i with source-origin distance r_{s_i} and azimuth θ_i , receiver location X with receiver-origin distance x , origin coordinate O , source–receiver distance $r_{s_i x}$, and the angle between source and receiver, φ_i , which is approximate to θ_i .

Table 1. Parameters of a four-layer model, modified from Luo *et al.* (2011).

Layer number	V_s (m s ⁻¹)	V_p (m s ⁻¹)	ρ (g cm ⁻³)	h (m)
1	400	800	2.0	10
2	200	400	2.0	10
3	600	1200	2.0	10
Half-space	800	1600	2.0	Infinite

We simulate the ambient seismic wavefield based on eq. (1) for explicit dispersion imaging comparisons. To make the simulations comparable, we use the same four-layer earth model parameters (presented in Table 1) and the same receiver recording configurations (100 traces, 1 m spatial interval and 10 ms temporal sampling interval). The total noise duration is 15-min-long; the total source number is 200; all source impulses will be randomly emitted at every 20-s window. As for the source configuration, we consider two typical ambient source distribution models: a random source model and a linear source model. The temporal and spatial distribution of noise source will be further detailed, respectively.

2.1 Random ambient source distribution

In order to formulate the general passive surface wave imaging environment, we consider random sources that are uniformly surrounding the linear receiver array. Under the above general assumptions, eq. (1) becomes

$$\begin{aligned}
 u(x, \omega) &= \sum_{i=1}^{N_s} e^{j(\omega t_{s_i} - k_0 r_{s_i x})} \\
 &= \sum_{i=1}^{N_s} e^{j(\omega t_{s_i} - k_0 r_{s_i} - k_0 x \cos \theta_i)}. \quad (3)
 \end{aligned}$$

2.1.1 Non-interferometric passive surface wave methods

Cheng *et al.* (2018b) presented a review of the PMASW method (Park *et al.* 2004; Park & Miller 2008) and the ReMi method (Louie 2001; Xu *et al.* 2017) and indicated the equivalence of the dispersion imaging scheme between two techniques. The PMASW method uses a slant-stacking algorithm in the frequency–offset (f – x) domain and transfers the wavefield into the frequency–velocity (f – v) domain (Park *et al.* 1998, 2004). The ReMi approach first uses slant-stacking algorithm to transfer the offset–time (x – t) domain wavefield into the intercept–time–slowness (τ – p) domain (where τ indicates the intercept time and p indicates the slowness), then applies a Fourier transform to obtain an f – p domain dispersion image (e.g. Thorson & Claerbout 1985; Louie 2001; Xia *et al.* 2007). Shen *et al.* (2015) also demonstrated the resolution equivalence of these dispersion imaging methods for noise-free surface wave data. Therefore, we focus on the PMASW method to understand the non-interferometric dispersion imaging scheme, including the underlying physics and the approximation.

According to Park *et al.* (2004) and Park & Miller (2008), we apply the phase-shift method (Park *et al.* 1998) to transform the seismic wavefield $u(x, \omega)$ into dispersion spectra. We first calculate the phase spectrum of the ambient seismic wavefield as

$$\begin{aligned}
 \Phi(x, \omega) &= \frac{u(x, \omega)}{|u(x, \omega)|} \\
 &= \sum_{i=1}^{N_s} e^{j(\omega t_{s_i} - k_0 r_{s_i} - k_0 x \cos \theta_i)} \\
 &= \sum_{i=1}^{N_s} e^{j(\omega t_{s_i} - k_0 r_{s_i})} e^{-j k_0 x \cos \theta_i} \\
 &= \sum_{i=1}^{N_s} \Phi_{s_i} e^{-j k_0 x \cos \theta_i}, \quad (4)
 \end{aligned}$$

where $\Phi_{s_i} = e^{j(\omega t_{s_i} - k_0 r_{s_i})}$ is referred to as the source distribution term, associated with the time and spatial distribution of noise sources. For consistency, we present the dispersion spectra in the f – k domain as

$$\begin{aligned}
 E(k, \omega) &= \left| \sum_{n=1}^N e^{j k x_n} \frac{u(x_n, \omega)}{|u(x_n, \omega)|} \right| \\
 &= \left| \sum_{n=1}^N e^{j k x_n} \sum_{i=1}^{N_s} \Phi_{s_i} e^{-j k_0 x_n \cos \theta_i} \right| \\
 &= \left| \sum_{i=1}^{N_s} \Phi_{s_i} \sum_{n=1}^N e^{j(k - k_0 \cos \theta_i) x_n} \right|, \quad (5)
 \end{aligned}$$

where $E(k, \omega)$ is dispersion spectra for scanning wavenumber (k) and scanning angular frequency (ω); N is the total receiver number; x_n denotes the offset information of the n th receiver, relative to the first receiver or some pre-defined origin point.

We know that the summation of $e^{j(k - k_0 \cos \theta_i) x_n}$ has a maximum when k is approaching $k_0 \cos \theta_i$. Given we could ignore the source distribution term Φ_{s_i} , in extreme cases all noise sources are uniformly distribution in both spatial and temporal domain (Figs S1a–c), we can further formulate the dispersion

spectra as

$$E(k, \omega) \approx \left| \sum_{i=1}^{N_s} \sum_{n=1}^N e^{j(k-k_0 \cos \theta_i)x_n} \right| \\ = \sum_{i=1}^{N_s} P_i(k(w) - k_0(w) \cos \theta_i), \quad (6)$$

where $P_i(k)$ is a positive function of wavenumber and has a peak when $k = 0$. Eq. (6) produces a complex dispersion energy image which consists of multiple peaks $k_0(w) \cos \theta_i$ at each frequency. Each peak can be taken as an apparent wavenumber associated with the source located at azimuth θ_i , and the energy at each pixel of the dispersion image represents the probabilities of various peaks considering the modal superposition property of surface waves (Aki & Richards 2002). Given θ is uniformly distributed from 0 to 2π , it is known that the probability density function (PDF) of a cosine function ($x = \cos \theta$) is an arcsine function ($f_\theta(x) = \frac{1}{\pi \sqrt{1-x^2}}$) (Fig. S2) which possesses the highest probability when $|x = \cos \theta|$ is approaching 1 (Ushakov 2001; Stirzaker 2003). Therefore, the dispersion energy image obtained from eq. (6) will show the highest probability/peak when k is approaching $k_0 \cos \theta = k_0$ (the true wavenumber) at each frequency.

Considering the source distribution term was omitted, eq. (6) presents the approximate solution of eq. (5) and illuminates the underlying physics of non-interferometric passive surface wave methods. Unfortunately, the condition to fulfil the approximation is rarely achievable in practice, and so is eq. (6). Instead, the source distribution term Φ_{S_i} will smear the dispersion energy image and prevents the energy peaks function $P_i(k)$ from converging at k_0 . Fig. 3 presents two numerical examples to exhibit comparisons between the original (eq. 5) and approximate (eq. 6) solutions of non-interferometric method on random source distribution models. In the individual sources case (Fig. 3a), both dispersion measurements (Figs 3b and c) show 5 energy peaks at each frequency which is associated with the defined 5 individual sources. Note that, with the existence of the source distribution term, the observed multiple energy peaks on the original measurement (Fig. 3b) are messy and a bit off the predicted apparent wavenumber $k_0(w) \cos \theta_i$. In the total 200 sources case (Fig. 3d), the original measurement (Fig. 3e) shows a section of messy energy below the theoretical dispersion curve (the blue dash line) instead of converging at the theoretical dispersion curve as the approximate measurement (Fig. 3f).

In order to enhance the dispersion spectra, the time ensemble averaging, a typical data processing technique used in seismic interferometry (Bensen *et al.* 2007; Weemstra *et al.* 2014; Cheng *et al.* 2018a), is usually applied to the non-interferometric passive surface wave methods (Fig. 1). By applying time ensemble averaging, the continuous and large-duration ambient seismic records will be divided into many short-window time segments and dispersion spectra will be measured and stacked for all segments to attenuate effects from the source distribution term Φ_{S_i} . We indicate this ensemble averaging using the notation $\langle \dots \rangle$, then rewrite eq. (5) as

$$\langle E(k, \omega) \rangle = \left\langle \left| \sum_{i=1}^{N_s} \Phi_{S_i} \sum_{n=1}^N e^{j(k-k_0 \cos \theta_i)x_n} \right| \right\rangle, \quad (7)$$

where $\langle E(k, \omega) \rangle$ indicates the ensemble stacked dispersion spectra.

According to the numerical observations on Fig. 3, eq. (5) will not converge at the theoretical wavenumber $k_0(w)$ as eq. (6), but presents as multiple apparent wavenumbers $k_0(w) \cos \psi$, where $\cos \psi$ is an arbitrary coefficient that is not equal to $\cos \theta_i$ due to the existence of the non-negligible source distribution term [see the biases between

the predicted apparent dispersion curves ($k_0(w) \cos \theta_i$) and the multiple energy peaks in Fig. 3b]. With the ensemble stacking of multiple dispersion spectra from each short-window time segment, the highest probability/peak of the ensemble stacked dispersion spectra can be tracked with the PDF of these apparent wavenumbers $k_0(w) \cos \psi$. Since $\cos \psi$ will not reach 1, $\langle E(k, \omega) \rangle$ from the original measurements will eventually converge at somewhere close to the theoretical wavenumber $k_0(w)$ due to the monotony property of the PDF function (Fig. S2). Based on above analysis, we can implicitly express the final peaks of $\langle E(k, \omega) \rangle$ as

$$\arg \max_{(k, \omega)} \langle E(k, \omega) \rangle \approx k_0(w) \cdot C, \quad (8)$$

where C is a constant with a value smaller than but close to 1, and varies with site and receiver geometry. Note that the directional ambient source effects might introduce frequency-dependent C values due to the source characteristics, which is not examined in this work due to the complexity; more details will be further discussed later. In some degree, $k_0(w) \cdot C$ can be taken as the ‘dominant’ apparent wavenumber over the time ensemble period. Eq. (8) indicates the real ability of non-interferometric methods, that the dispersion measurements will be usually biased from the accurate dispersion information in practice. The biased measurements usually present with the lower wavenumber peaks or higher apparent velocity peaks in terms of the accurate values. The ensemble stacked dispersion spectra from eq. (6) would converge at the theoretical wavenumber only if the source distribution term can be omitted. A special case might fulfil this condition that the noise sources are homogeneously distributed along a single radius ($r_i = 3$ km) and emitted at a uniform time ($t_{S_i} = 0$; Fig. S1).

We presents a numerical example to explicate the comparison between the original (Fig. 4a) and approximate (Fig. 4b) solutions of non-interferometric method after 15-min time-averaged ensemble. The energy peaks of the original measurement are close to but still a bit off the theoretical dispersion curve, which stands at the top boundary of the apparent wavenumber energy; while the energy peaks of the approximate measurement appear much cleaner and closely follow the theoretical dispersion curve. These numerical observations are consistent with the analyses above.

2.1.2 Interferometric passive surface wave methods

Several studies have argued on the advantages of interferometric passive surface wave methods in contrast with non-interferometric methods (O’Connell & Turner 2011; Le Feuvre *et al.* 2015; Hayashi *et al.* 2015; Cheng *et al.* 2016, 2018b; Xu *et al.* 2017). In order to reveal the underlying differences, we follow the same assumptions to build the Green’s function approximations and the dispersion imaging schemes for the MAPS and SPAC methods.

We follow the conventions in Sánchez-Sesma & Campillo (2006) with two records [$u(x_m, \omega)$ and $u(x_n, \omega)$] as described in eq. (3), and present the cross-correlation spectrum C_{x_m, x_n} as

$$C_{x_m, x_n} = u(x_m, \omega) u^*(x_n, \omega) \\ = \sum_{i=1}^{N_s} e^{-jk_0(r_{S_i x_m} - r_{S_i x_n})} + \overline{C_{x_m, x_n}}, \quad (9)$$

where $*$ denotes the complex conjugate; $\overline{C_{x_m, x_n}}$ is the cross term,

$$\overline{C_{x_m, x_n}} = \sum_{m=1}^{N_s} e^{j(\omega t_{S_m} - k_0 r_{S_m x_m})} \sum_{n=1}^{N_s} e^{-j(\omega t_{S_n} - k_0 r_{S_n x_n})} \quad (m \neq n). \quad (10)$$

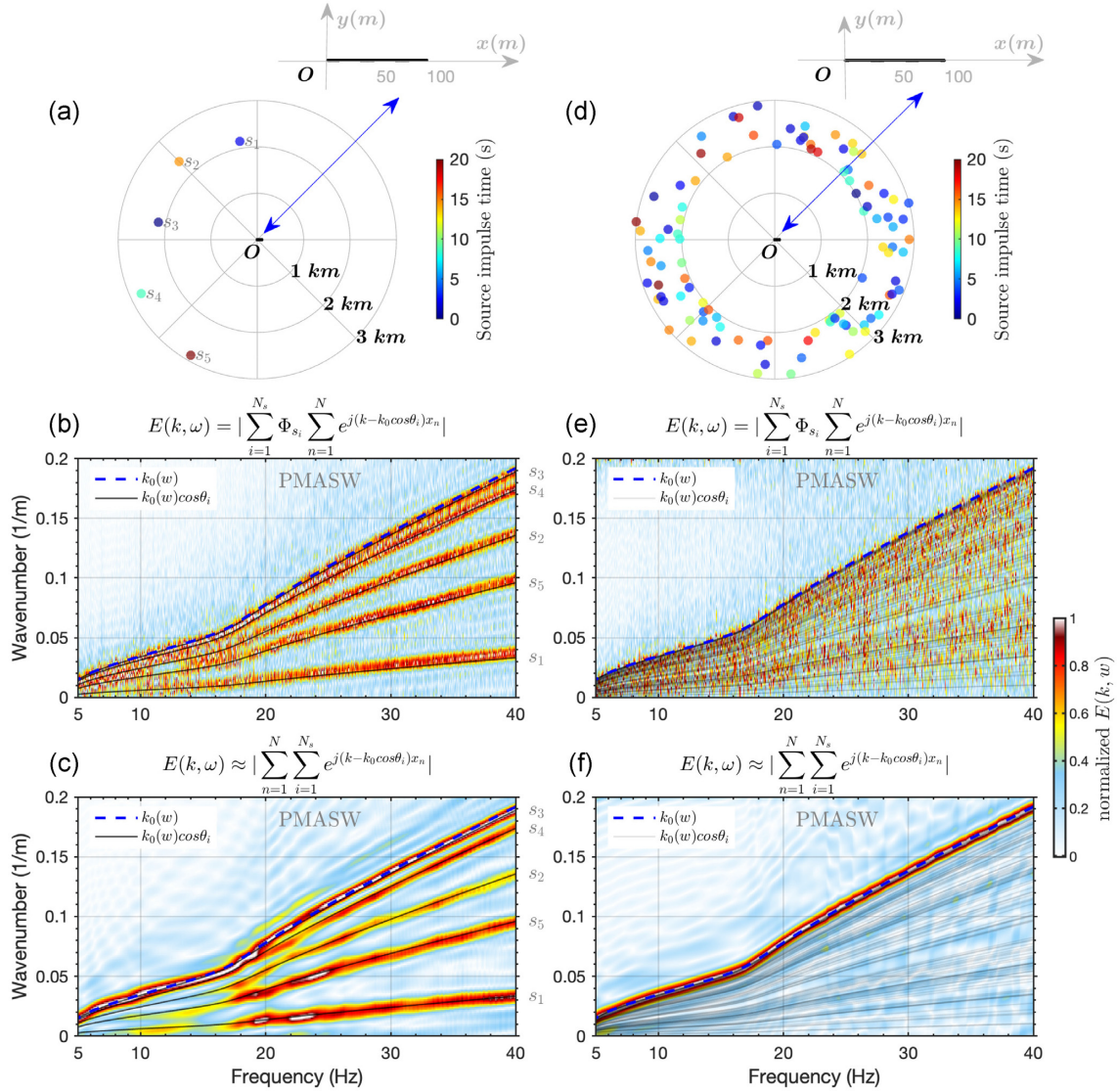


Figure 3. Comparisons between original and approximate solutions of non-interferometric method (PMASW) over one segment (20 s) on random source distribution models, including the individual sources case (left-hand panels a, b, c) and the total sources case (right-hand panel d, e, f). (a) Source–receiver configuration of the individual sources case (the colour coded by the random source impulse time); panels (b) and (c) dispersion spectra measured by the original and approximate solutions of non-interferometric method (PMASW); (d) source–receiver configuration with the total sources case (the colour coded by the random source impulse time); panels (e) and (f) dispersion spectra measured by the original and approximate solutions of non-interferometric method (PMASW). The dashed lines display the theoretical dispersion curves $k_0(\omega)$ calculated by Knopoff’s method (Schwab & Knopoff 1972); the thin solid lines show the apparent dispersion curves $k_0(\omega)\cos\theta_i$, where θ_i is associated with the azimuth of the corresponding source. The individual sources case includes only 5 random sources as labelled with s_i , $i = 1, 5$; the total sources case includes the total 200 random sources.

In most analytical derivations of the noise cross-correlation function, noise sources are assumed to be uncorrelated in time and space, and the contribution of each source to the cross-correlation function could be determined independently (Tromp *et al.* 2010; Lawrence *et al.* 2013). It suggests that the cross term $\langle C_{x_m, x_n} \rangle$ could be negligible with a sufficiently time-averaged ensemble. According to the geometric relationship in eq. (2) with the far-field approximation, we get the relationship, $r_{s_i x_m} \approx r_{s_i x_n} + x_{mn} \cos\theta_i$. Substituting this into eq. (9) and applying ensemble averaging yields

$$\begin{aligned} \langle C_{x_m, x_n} \rangle &\approx \left\langle \sum_{i=1}^{N_s} e^{-j k_0 \cos\theta_i x_{mn}} \right\rangle \\ &\approx J_0(k_0 x_{mn}), \end{aligned} \quad (11)$$

where J_0 is the order zero Bessel function of the first kind; x_{mn} denotes the inter-station distance between two receivers located at x_m and x_n , respectively. The derivation of J_0 was found by Aki (1957) in the framework of microtremors with an integral representation over azimuthal from 0 to 2π . The transition from an integral to the discrete summation limits this equation under the scope of uniform ambient noise source distribution cases. Eq. (11) simplifies the cross-correlation function into the analytical solution of Sánchez-Sesma & Campillo (2006) which expresses the linear relationship between the real part of the cross-correlation spectrum $\langle C_{x_m, x_n} \rangle$ and the imaginary part of the Green’s function (the Bessel function J_0) between two receivers. Therefore, we can easily derive the SPAC representation with the whitened cross-correlation function, which is also called cross-coherence function in ambient noise

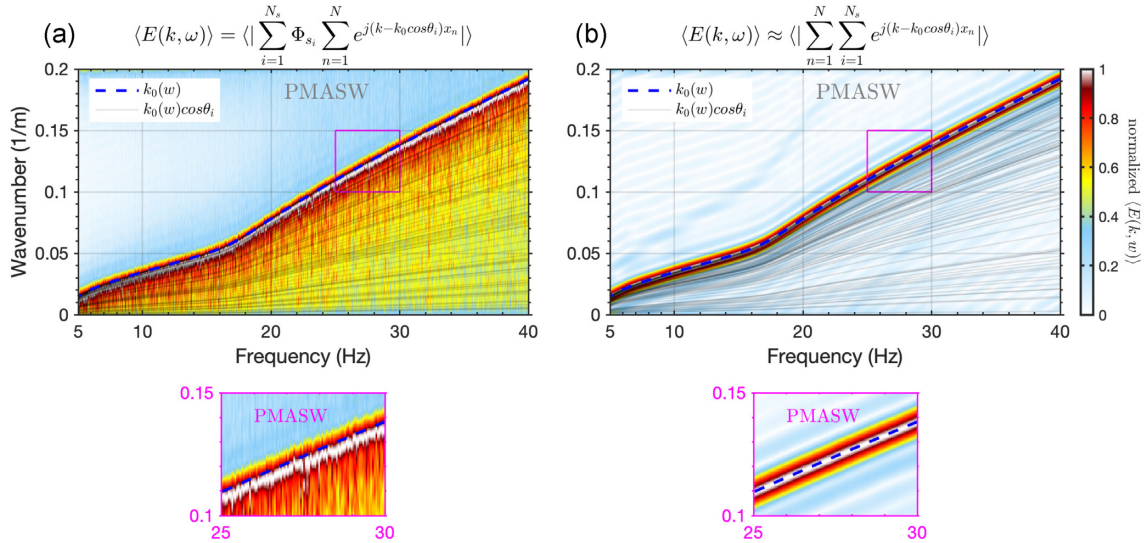


Figure 4. Comparison between original (a) and approximate (b) solutions of non-interferometric method (PMASW) over 15 min time-averaged ensemble on the total 200 random sources distribution model. For better comparison, the highlighted windows on a and b are zoomed-in displayed at bottom.

interferometry literatures (Prieto *et al.* 2009; Tsai & Moschetti 2010; Lawrence & Prieto 2011; Weemstra *et al.* 2014).

We use the slant-stacking algorithm (Park *et al.* 1998) by replacing the wavefield $u(x, \omega)$ in eq. (5) with ensemble averaged cross-correlation wavefield $\langle C_{x_m, x_n} \rangle$ to obtain the MAPS representation

$$\begin{aligned}
 \langle E(k, \omega) \rangle &= \left| \sum_{m=1}^{N-1} \sum_{n=m+1}^N e^{jkx_{mn}} \frac{\langle C_{x_m, x_n}(x_{mn}, \omega) \rangle}{|\langle C_{x_m, x_n}(x_{mn}, \omega) \rangle|} \right| \\
 &\approx \left| \sum_{m=1}^{N-1} \sum_{n=m+1}^N e^{jkx_{mn}} \sum_{i=1}^{N_s} e^{-jk_0 \cos \theta_i x_{mn}} \right| \\
 &= \left| \sum_{m=1}^{N-1} \sum_{n=m+1}^N e^{jkx_{mn}} J_0(k_0 x_{mn}) \right|. \quad (12)
 \end{aligned}$$

With the random noise source distribution, the interferometric method (eq. 12) only requires sufficient time-averaged ensemble to cancel out the cross term and produce the accurate dispersion curve information, instead of depending on the ideal homogeneous source distribution hypothesis as the non-interferometric method (eq. 6).

In order to present the effects from the cross term on dispersion imaging, we use similar numerical tests on interferometric method to compare the original and approximate solutions before time-averaged ensemble (Fig. 5). For either the individual sources case or the total sources case, both original and approximate dispersion measurements present the accurate energy peaks as predicted by the theoretical wavenumbers (highlighted by the blue dashed lines) and the apparent wavenumbers (highlighted by the black solid lines), but the cross term existing in the original dispersion measurements produces lots of artefacts and pollutes the dispersion energy images. Whereas, after 15 min time-averaged ensemble, the original dispersion image turns to be rather cleaner with the cross term significantly cancelled out as shown on Fig. 6. We also present two zoomed-in windows on the original and approximate dispersion images to highlight the accuracy of the interferometric method.

2.2 Roadside (in-line) ambient source distribution

Realistic source fields can be far from uniform (Stehly *et al.* 2006; Kedar *et al.* 2008; Landès *et al.* 2010; Hillers *et al.* 2012). With the increasing necessity of surveys within urban areas, passive surface wave methods utilizing the traffic-induced ambient sources along roadside profiles provide an ideal geometry from a logistics perspective as discussed in past studies (Louie 2001; Okada & Suto 2003; Park *et al.* 2004; Cheng *et al.* 2015, 2018a). In the case of a survey line alongside a road, the ambient sources are usually generated by moving vehicles on the surface of the road. If the road is fairly straight and of reasonable extent (in subsequent examples, 10 times or more the array length), the ambient seismic records observed by the linear array alongside the road can be typically considered as in-line plane waves.

Given that the near-field effect is negligible, the geometrical relationship of the far-field approximation for the in-line source distribution becomes $r_{s_i, x} = r_{s_i} + x$. Replacing $r_{s_i, x}$ in eq. (3), the ambient seismic wavefield for the in-line source distribution can be written as

$$\begin{aligned}
 u(x, \omega) &= \sum_{i=1}^{N_s} e^{j(\omega t_{s_i} - k_0 r_{s_i} - k_0 x)} \\
 &= e^{-jk_0 x} \sum_{i=1}^{N_s} e^{j(\omega t_{s_i} - k_0 r_{s_i})}. \quad (13)
 \end{aligned}$$

2.2.1 Non-interferometric passive surface wave methods

We can modify the dispersion spectra of eq. (5) for the non-interferometric methods as,

$$\begin{aligned}
 E(k, \omega) &= \left| \sum_{n=1}^N e^{jkx_n} \frac{u(x_n, \omega)}{|u(x_n, \omega)|} \right| \\
 &= \left| \sum_{n=1}^N e^{j(k-k_0)x_n} \sum_{i=1}^{N_s} e^{j(\omega t_{s_i} - k_0 r_{s_i})} \right| \\
 &= \left| \sum_{n=1}^N e^{j(k-k_0)x_n} \Phi \right|, \quad (14)
 \end{aligned}$$

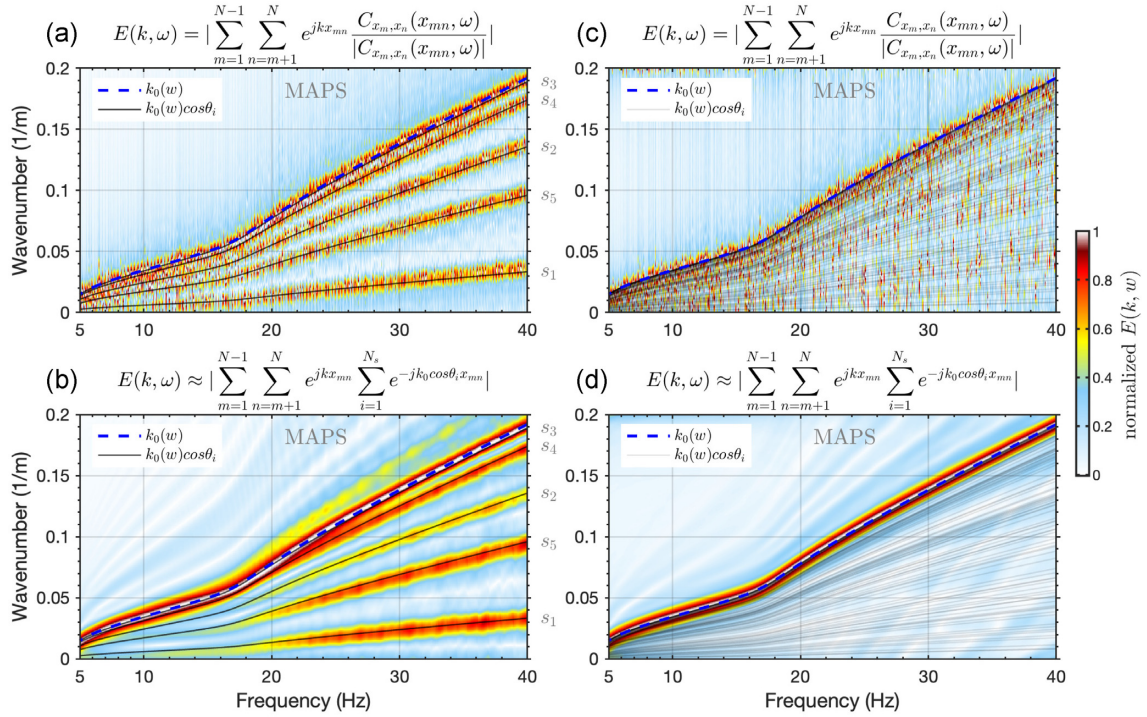


Figure 5. Comparisons between original and approximate solutions of interferometric method (MAPS) over one segment (20 s) on random source distribution models, including the individual sources case (left-hand panel, a and b) and the total sources case (right-hand panel, c and d). Panels (a) and (b): dispersion spectra measured by the original and approximate solutions of interferometric method (MAPS) under the individual sources case; panels (c) and (d): dispersion spectra measured by the original and approximate solutions of interferometric method (MAPS) under the total sources case. Source-receiver configurations of both cases are the same as that on Fig. 3.

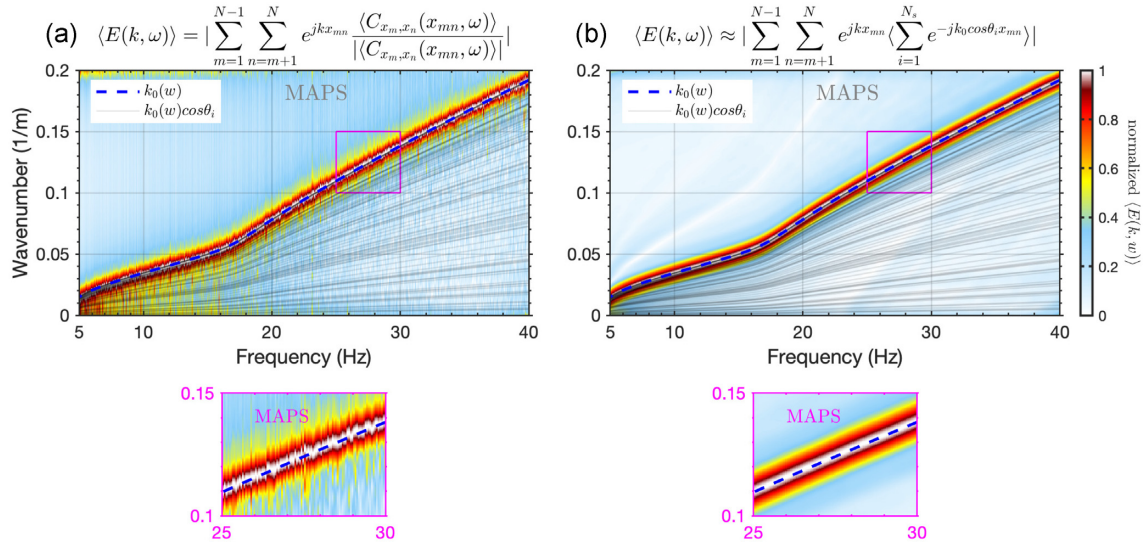


Figure 6. Comparison between original (a) and approximate (b) solutions of interferometric method (MAPS) over 15-min time-averaged ensemble on the total 200 random sources distribution model. The highlighted windows on (a) and (b) are zoomed-in displayed at bottom for better comparison.

where $\bar{\Phi} = \sum_{i=1}^{N_s} e^{j(\omega t_{s_i} - k_0 r_{s_i})}$ indicates the ensemble source distribution term, which contributes as random noise on dispersion spectra and will converge to a constant value with sufficient time-averaged ensemble. Therefore, we can further simplify eq. (14) as

$$\langle E(k, \omega) \rangle \approx \left\langle \left| \sum_{n=1}^N e^{j(k-k_0)x_n} \right| \right\rangle. \quad (15)$$

Eq. (15) explains the underlying physics for roadside non-interferometric passive surface wave methods. Under the in-line source distribution hypothesis, non-interferometric passive surface wave methods finally derive out an ensemble-averaged dispersion measurement though a series of MASW measurements with the corresponding sources located around the first Fresnel zone. However, due to the existence of the off-line sources, the ensemble-averaged dispersion measurement will usually appear smeared compared to a real MASW measurement considering the same frequency target.

2.2.2 Interferometric passive surface wave methods

Substituting eq. (13) into eq. (9), and applying ensemble averaging, yields the updated cross-correlation spectrum $\langle C_{x_m, x_n} \rangle$ under the in-line source distribution

$$\begin{aligned} \langle C_{x_m, x_n} \rangle &= \langle u(x_m, \omega) u^*(x_n, \omega) \rangle \\ &= \left\langle \sum_{i=1}^{N_s} e^{-jk_0 x_{mn}} + \overline{C_{x_m, x_n}} \right\rangle \\ &\approx e^{-jk_0 x_{mn}}. \end{aligned} \quad (16)$$

Therefore, we can update the MAPS representation for the roadside passive surface wave survey as

$$\begin{aligned} E(k, \omega) &= \left| \sum_{m=1}^{N-1} \sum_{n=m+1}^N e^{jkx_{mn}} \frac{\langle C_{x_m, x_n}(x_{mn}, \omega) \rangle}{|\langle C_{x_m, x_n}(x_{mn}, \omega) \rangle|} \right| \\ &= \left| \sum_{m=1}^{N-1} \sum_{n=m+1}^N e^{j(k-k_0)x_{mn}} \right|. \end{aligned} \quad (17)$$

Eq. (17) is able to produce accurate dispersion curve. It also indicates the potential to apply interferometric passive surface wave methods to active surface wave data to improve coherent signal quality (Li & Li 2018), but the impact of potential spurious higher modes should also be aware (Halliday & Curtis 2008).

As for the roadside passive surface wave method, the only assumption is the in-line source distribution. Given the required in-line source distribution condition, eqs (14) and (17) demonstrate the possibility of both non-interferometric and interferometric passive surface wave methods to produce accurate dispersion curve based on the linear receiver array. Compared with the ideal homogeneous source distribution condition, the in-line source distribution is more achievable although challenges still exist. To avoid interfering with traffic flow, the linear receiver arrays are usually deployed a bit off from the main road (i.e. off-line from the actual traffic). As a result, the in-line source distribution condition may not hold because the traffic is not directly in-line with the receiver array; this indicates that the assumptions in eq. (14) will not be perfectly satisfied. The non-interferometric dispersion measurement will degrade from eq. (14) to eq. (8), which will introduce a bias. Generally, the interferometric methods will still be able to retrieve accurate dispersion information in a wide range even based on eq. (12).

Fig. 7 presents comparisons between non-interferometric and interferometric methods for a linear source distribution with different off-line distances. When the off-line distance ($dh = 10$ m) is small enough, that is 10 per cent of the array length ($L = 100$ m), and the source distribution length ($L_S = 3000$ m) is much larger than the array length (Fig. 7a), the in-line source distribution condition usually holds. Therefore, both PMASW measurement (Fig. 7b) and MAPS measurement (Fig. 7c) are able to approach the theoretical dispersion curve. If the off-line distance ($dh = 100$ m) is comparable with the array length ($L = 100$ m), however, the in-line source distribution condition will break, resulting in incorrect dispersion curve estimation. PMASW produces biased/lower energy peaks (Fig. 7e) but MAPS still recovers the expected result (Fig. 7f). We also present the zoomed-in windows on the observed dispersion images to highlight the accuracy of the interferometric method (the green and red boxes), as well as the biases of the non-interferometric method (the cyan and magenta boxes). Note that we do not present more analysis on the specific parameter settings for the roadside passive surface wave survey, such as the off-line distance limits, array orientation

(parallel or perpendicular to the road line) influences, observation duration, etc. which are beyond the scope of this work.

2.3 Bias estimation for non-interferometric methods

Louie (2001) indicated that an interpreter must pick the lower edge of energy peaks of phase velocities, rather than the peaks, and hypothesized that the off-line triggered sources caused the higher apparent velocities. In this sense, the ReMi approach and similar techniques seek to pick the lower bound of apparent velocities so as to attenuate the dispersion bias associated with waves travelling broadside to the array. In fact, this off-line source distribution is only the tip of the iceberg; this bias phenomenon is not unique to the ReMi method but is relevant to all linear-array-based non-interferometric passive surface wave methods.

We have demonstrated two basic assumptions of non-interferometric passive surface wave methods: (i) homogeneous distribution of distant sources and (ii) dominant in-line sources distribution. These assumptions are satisfied in many numerical ReMi related studies (Louie 2001; Pullammanappallil *et al.* 2003; Strobbia & Cassiani 2011; Strobbia *et al.* 2015). However, both assumptions are rarely satisfied in practice as we detailed previously, which will inevitably cause velocity overestimation or wavenumber underestimation (eq. 8). Louie (2001) and Pancha *et al.* (2008) provided some rules of thumb for picking the minimum apparent velocities, like detecting the ‘best guess’ velocity where spectral ratio is changing steeply. Strobbia & Cassiani (2011) also developed an inversion algorithm using existing receiver array information and a hypothetical uniform source distribution to identify the lowest apparent velocity.

Eq. (8) mathematically explains the potential biases caused by invalid assumptions about the nature of the ambient wavefield. We do not solve for the specific value of C , because it varies with the source characteristic in site and the receiver array geometry. Given a fixed receiver array, the measured dispersion spectra from eq. (5) at individual time segment will vary with the individual source distribution, however, we know that there is no possibility to underestimate apparent velocity. It means the accurate dispersion curve will always stand at the top boundary of the apparent wavenumber energy for each individual dispersion spectral image (Fig. S3). This argument about there is no lower apparent velocities is also the underlying rules to pick the spectrum boundary or the steepest gradient of the dispersion curve envelope given by Louie (2001). Therefore, it is possible to estimate the bias of the measurement using a kind of attribute for the boundary indicator, which is similar to imaging resolution; a higher imaging resolution means a thinner boundary zone, as well as smaller bias, and vice versa.

Here we use the array response function (ARF), which is a property of the acquisition array and the spectral estimator (Birtill *et al.* 1965; Johnson & Dudgeon 1993; Boiero & Socco 2011; Bergamo *et al.* 2012; Ruigrok *et al.* 2017), to present the imaging resolution. Similar to the slant-stacking-based dispersion imaging methods, for example PMASW and ReMi, we define the ARF as:

$$W(k) = \sum_{n=1}^N e^{j(k-k_0)x_n}. \quad (18)$$

Fig. 8(a) shows normalized ARFs for two linear arrays with the same trace number $N = 50$, but different array lengths, $L = 50$ m (the deep pink line) and $L = 250$ m (the dark slate grey line). The main lobe of the ARF determines the imaging resolution, which is controlled by the array length L . In general, the longer array length captures higher resolution spectral imaging, and vice versa.

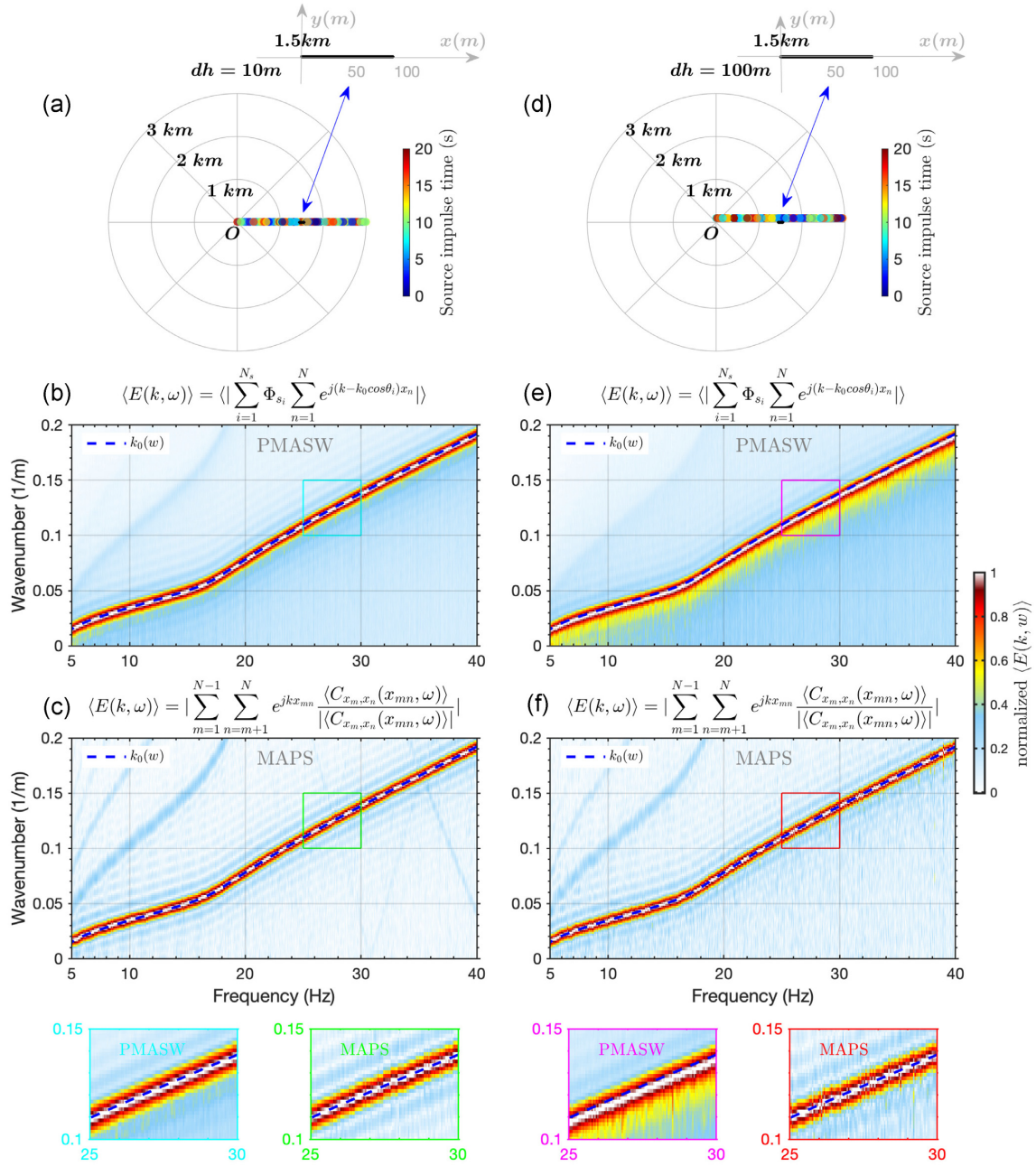


Figure 7. Comparisons between non-interferometric and interferometric methods on linear source distribution models with different off-line distances $dh = 10\text{ m}$ (left-hand panel, a, b, c) and $dh = 100\text{ m}$ (right-hand panel, d, e, f). (a) Source–receiver configuration with the linear source distribution at off-line distance $dh = 10\text{ m}$; panels (b) and (c): dispersion spectra measured by non-interferometric method (PMASW) and interferometric method (MAPS). (d) Source–receiver configuration with the linear source distribution at off-line distance $dh = 100\text{ m}$; panels (e) and (f): dispersion spectra measured by non-interferometric method (PMASW) and interferometric method (MAPS). The highlighted windows on (b), (c), (e) and (f) are zoomed-in displayed at bottom for better comparison. Note that the dispersion images are measured over 15 min time-averaged ensemble as signed by $\langle E(k, \omega) \rangle$ on the caption equation of each subfigure.

The imaging resolution or the width of the main lobe also indicates the bias between accurate wavenumber and the measured spectral peaks. Figs 8(b) and (c) present two model tests with the same source configuration defined in Fig. 7(d) and two different receiver arrays defined in Fig. 8(a). With different receiver arrays and different ARFs, PMASW measurements present different biases from the theoretical values (the dashed lines in Figs 8b and c). Note that the accurate wavenumber at 17 Hz (the thin black lines in b and c) do not intersect the peaks of the vertical resolution curves due to the biases. In detail, for frequency samples at 17 Hz, the shorter array

observes wavenumber bias $\varepsilon_s = 3.3e - 3\text{ m}^{-1}$ which is located at about 96.5 per cent ARF peak (as indicated by the thin black line in Fig. 8b); the longer array observes wavenumber bias $\varepsilon_l = 1.0e - 3\text{ m}^{-1}$ which is located at about 90.5 per cent ARF peak (as indicated by the thin black line in Fig. 8c). In fact, picking the spectrum boundary or the steepest gradient can not get rid of these biases (Fig. S4). Therefore, it is significant to estimate the bias of the measurements, and we offer a simple alternative in this work.

According to the Rayleigh resolution criterion (Johnson & Dudgeon 1993; Boiero & Socco 2011), we can use half of the ARF peak

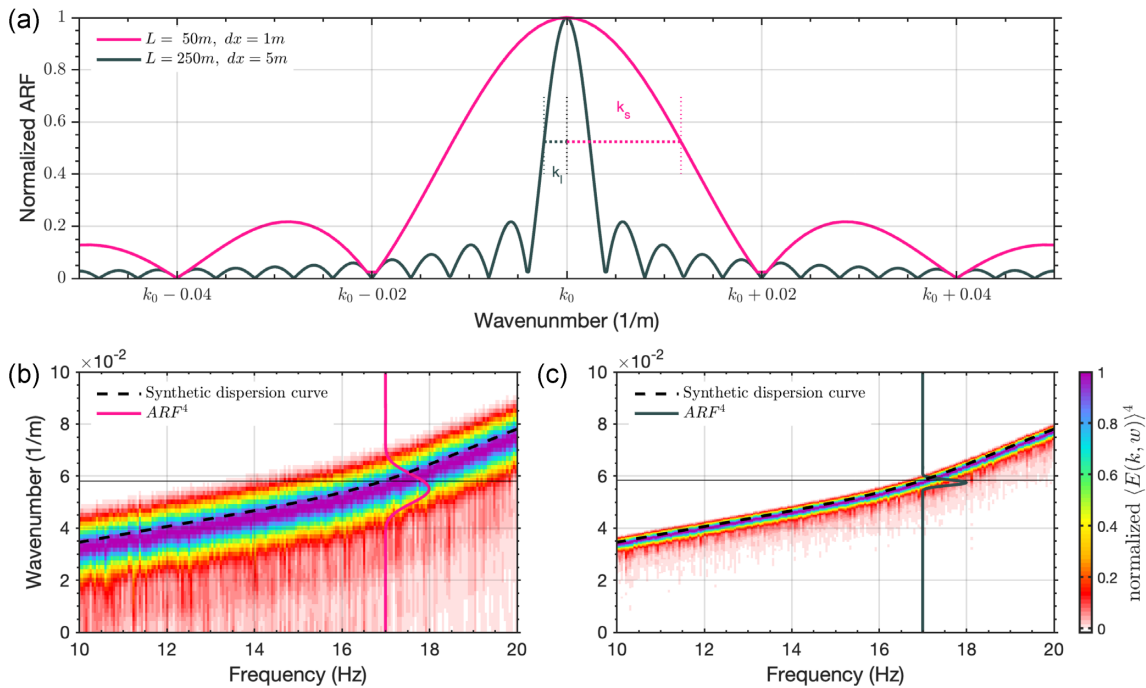


Figure 8. (a) Array smoothing functions for two linear arrays with different array lengths, $L = 50$ m (the pink line) and $L = 250$ m (the grey line). The dashed windows indicate the imaging resolutions for the longer array (k_l) and the shorter array (k_s). Panels (b) and (c): dispersion spectra (PMASW) for two linear arrays with different array lengths $L = 50$ m (b) and $L = 250$ m (c). The black dashed lines in (b) and (c) are the theoretical dispersion curves. The thick solid lines in (b) and (c) are the corresponding array smoothing functions which have been gained with fourth power (ARF^4) to be comparable with the gained dispersion spectra ($(E(k, \omega)^4)$) for better display. The thin black lines in (b) ($L = 50$ m) and (c) ($L = 250$ m) indicate the corresponding wavenumber locations at frequency 17 Hz.

(k_h) to quantify the imaging resolution as indicated by the dashed windows in Fig. 8(a). The measured biases of non-interferometric methods should be within the imaging resolution range ($0 < \varepsilon < k_h$). Therefore, we suggest k_h as a bias indicator during the interpretation of non-interferometric passive surface wave methods. For examples, we can calculate k_h values for all frequencies and use them as weights for dispersion curve inversion to normalize the observe dispersion curve data alternative to the standard deviation. Besides, people might also approximate the image resolution by directly using the geometry/offset information and the interested reader is referred to the works of Ruigrok *et al.* (2017).

For comparison, we also define the corresponding ARFs for interferometric methods. The MAPS method applies a slant-stack algorithm for dispersion imaging but uses C_N^2 cross-correlation pairs, so the ARF can be expressed as:

$$W(k) = \sum_{m=1}^{N-1} \sum_{n=m+1}^N e^{j(k-k_0)x_{mn}}. \quad (19)$$

Fig. 9 displays a comparison of array smoothing functions between different passive surface wave methods. Compared with the ARF of non-interferometric method, the ARF of interferometric method shows smoother side lobes due to the increased C_N^2 interstation pairs. The smoother side lobes decrease the possibility of the interference between the wiggles on ARF [or the array response artefacts (Wu *et al.* 2017; Cheng *et al.* 2021c)] and the incoherent noise. This might be one reason for the higher quality dispersion measurement produced by the interferometric methods compared to that by non-interferometric methods. Note that interferometric methods based on a single virtual source gather (N or $N - 1$ interstation pairs) will not have this advantage.

3 FIELD EXAMPLES

We present three typical field examples with different observation systems (e.g. instrument, receiver configuration, site environment) to further demonstrate comparisons between different passive surface wave methods. We applied the same data processing workflow, as illuminated in Fig. 1, on all three data sets. First, we split the continuous and long-duration ambient seismic records, usually around 10 min for urban passive surface wave survey, into short overlapped time segments. Based on our experiences, a 20-s window is good to ensure sufficient noise sources propagation range, as well as the efficiency of the ensemble averaging/stacking; too large stack count will increase computing costs. We apply 75 per cent overlap on each segment. To remove potential near-field interferences and whiten noise spectrum, we apply basic data pre-processing, including removing the mean, linear trend, dead traces, as well as instrument response as necessary, temporal normalization, spectral whitening and tapering two ends, for each individual time segment. Next, we directly apply non-interferometric dispersion measurements, for example PMASW and ReMi, on preprocessed time segments, while for interferometric methods we calculate empirical Green's function between each interstation pair.

In this work, we choose to use the whitened cross-correlation algorithm (Prieto *et al.* 2009; Weemstra *et al.* 2014) for MAPS for better comparison with SPAC method. Prior to picking the dispersion curve, non-interferometric methods stack all dispersion spectra together to improve the dispersion image quality, while interferometric methods stack all interferograms together before dispersion measurement to ensure the in-coherent noise, as well as cross terms (eq. 9), cancelled with sufficient ensemble averaging. Note that for interferometric methods, ensemble averaging/stacking needs to be done before the dispersion measurement, otherwise biases will be

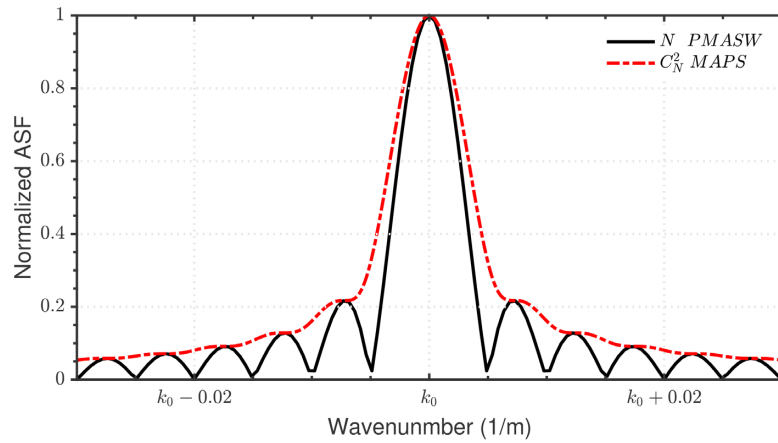


Figure 9. Array smoothing functions for different passive surface wave methods, non-interferometric method (PMASW, the black solid line), interferometric method (MAPS, the red dashed–dotted line).

introduced due to the existence of cross terms. All the dispersion spectral images measured with different passive surface wave methods are raised to the power of fourth $[E(k, \omega)^4]$ for better display. Besides the steps mentioned, we do not apply any special data processing approaches on individual measurements in order to allow better comparison between the techniques. However, improvement of the results would likely be possible through utilization of other techniques such as spectral de-spiking (Girard & Shrage 2019), time segment data-selection (Cheng *et al.* 2018b; Pang *et al.* 2019; Cheng *et al.* 2019), and related approaches. Considering either non-interferometric methods or interferometric methods are not sensitive to specific surface wave inversion techniques once dispersion curves are picked from the measured dispersion spectra, we only focus on surface wave dispersion measurement and do not include discussions or interpretations on surface wave inversion in this study. Besides, the SPAC method discussed in this study use the standard SPAC procedure, with the exception of the azimuthal average, to derive the dispersion curve by the inversion of spatial autocorrelation curves; other SPAC methods, like the direct-fitting method by Asten & Roberts (2006) and Asten & Hayashi (2018), might not fit the discussions in this study.

3.1 Field data set #1

Fig. 10 displays the photograph of the layout of data set #1, which is located inside the campus of Zhejiang university. A linear array of 38 Zland nodes (5 Hz) was deployed on a grassy plot; data were acquired at a 500 Hz sampling rate and 1 m spatial-interval. Five-min-long continuous ambient seismic records were acquired, and processed according to the previously described workflow and parameters. We only focus on the Z-component, which is relevant to Rayleigh waves, in the present analysis. We compare the dispersion measurements generated by different passive surface wave methods, PMASW (Fig. 11a), ReMi (Fig. 11b), MAPS (Fig. 11c) and SPAC (Fig. 11d). The black crosses indicate the picked dispersion curve based on the MAPS measurement.

In general, the interferometric methods provide much clearer spectral images, and their dispersion measurements are consistent with each other. However, the SPAC measurement provides lower sensitivity to higher modes. This is due to the fact that the classical SPAC method, as described by Aki (1957), is based on the assumption of a single-valued wavenumber component per frequency contained in the wavefield, which results in superposed modes rather

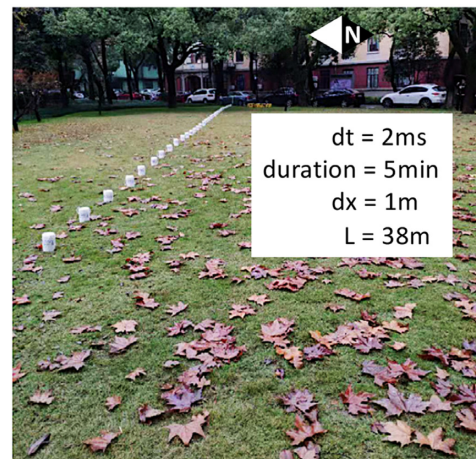


Figure 10. Photograph of field layout of data set #1 inside campus of Zhejiang university.

than individual modes when multiple modes exist (Cornou *et al.* 2006). To analyse the higher modes from SPAC method, one can calculate the theoretical effective phase velocities corresponding to the observed one (Asten & Roberts 1997; Ohori *et al.* 2002; O'Neill & Matsuoka 2005; Ikeda *et al.* 2012) or directly fit the theoretical SPAC coefficients with the observed SPAC coefficients (Asten *et al.* 2004, 2022; Asten 2006; Ikeda *et al.* 2012; Asten & Hayashi 2018; Hayashi *et al.* 2022). Besides, it is worth to mention that a similar technique, the frequency–Bessel transform, might be able to improve higher modes with an appropriate spectral decomposition on the frequency–Bessel spectrogram (Forbriger 2003; Wang *et al.* 2019; Hu *et al.* 2020; Xi *et al.* 2021).

In terms of computing cost, the MAPS method is more efficient than the SPAC method without the costs of Bessel functions evaluation. Compared with MAPS, both PMASW and ReMi measurements contain biased spectral peaks which is consistent with eq. (8), and noisy spectra which are likely caused by near-field incoherent noise from the road perpendicular to the observation line. Compared with the PMASW measurement, ReMi performs poorly in this case with a discontinuous higher mode. This results from the lower sensitivity of the time-domain slant-stack algorithm for frequency variations at extremely high apparent velocities. Generally, the τ – p transform breaks down in resolution along the frequency axes as well as velocity axes when surface waves with different

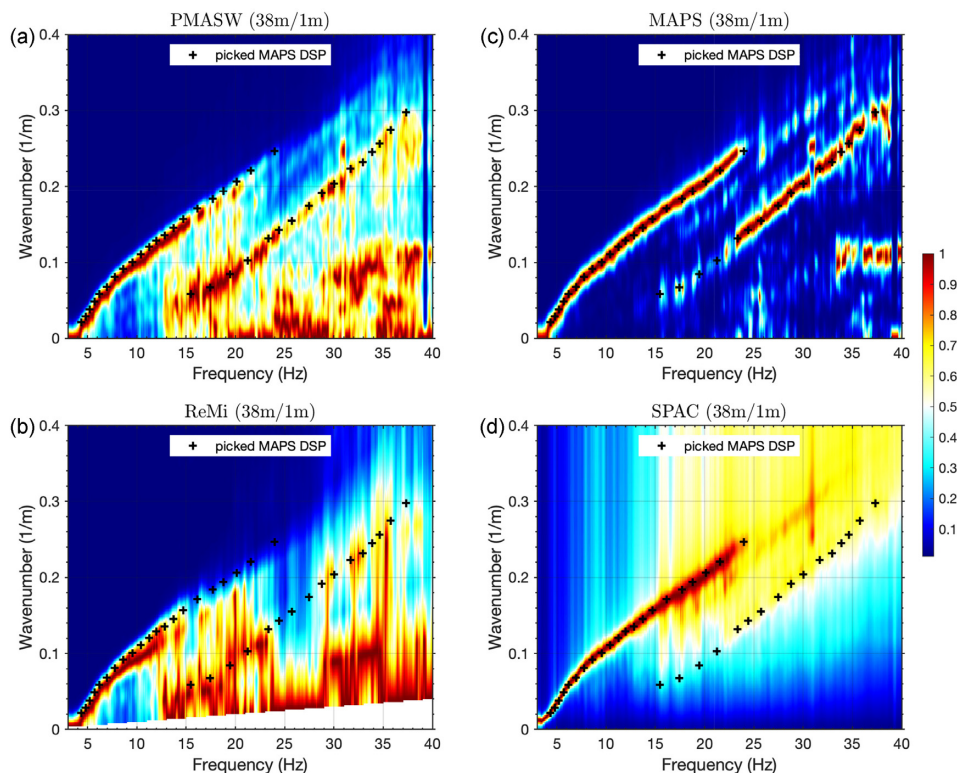


Figure 11. Measured dispersion spectra based on data set #1 with different passive surface wave methods, PMASW method (a), ReMi method (b), MAPS method (c) and SPAC method (d). The black crosses indicate the picked dispersion curve from MAPS measurement. Note that, we limited wavenumber ($0\text{--}0.4\text{ m}^{-1}$) below the Nyquist wavenumber ($1/dx/2 = 0.5\text{ m}^{-1}$) to better display the performances of different methods considering the measurements from the non-interferometric methods (PMASW and ReMi) are noisy.

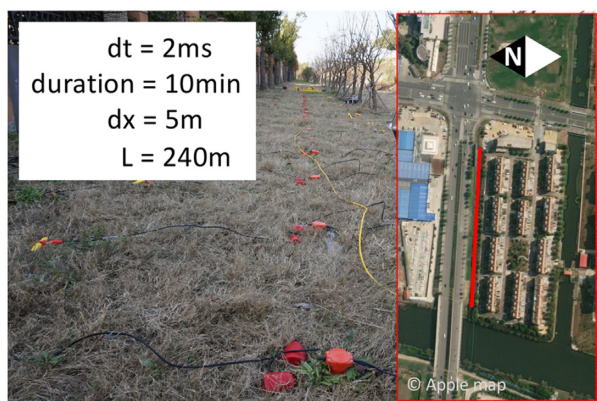


Figure 12. Site map of data set #2 with the receiver array along the Zhaoxia Road in Nantong city.

frequencies and phase velocities are superimposed (Park *et al.* 1998). In this way, PMASW is superior to ReMi due to its algorithmic advantage from the frequency-domain slant-stacking, which is also the reason why the phase-shift method (Park *et al.* 1998) is more popular and computationally efficient than the conventional τ - p transform method (McMechan & Yedlin 1981) for MASW imaging.

3.2 Field data set #2

Fig. 12 displays the site map of data set #2. A linear array of 48 RefTek 125A digitizers connected to 2.5 Hz vertical-component

geophones was deployed along the Zhaoxia Road in Nantong city. Continuous ambient seismic data (10-min records) were recorded with a 2 ms sampling interval and 5 m spatial interval. The previously described workflow and parameters were then applied for data analysis. An active surface wave (MASW) survey was simultaneously performed along the observation line with a Geometrics Geodes equipped with 48 2.5 Hz vertical-component geophones. The sampling interval for active surface wave survey is 0.25 ms and the receiver interval is 1 m. A 6.3 kg (~ 14 lbs) sledge hammer was utilized as an active source with a nearest offset of 10 m. Fig. 13 presents a comparison between the different passive surface wave methods, PMASW (Fig. 13a), ReMi (Fig. 13b), MAPS (Fig. 13c) and SPAC (Fig. 13d).

Except for the higher imaging resolution, all four methods generally present similar response for this data set as they do in data set #1. Compared with data set #1, the receiver array is longer (240 m versus 38 m) which results in higher imaging resolution ($k_h = 2.3e - 3\text{ m}^{-1}$) based on eq. (18). We observe smaller biases between interferometric measurements and non-interferometric measurements. Here we can take the imaging resolution, k_h , as an error factor for the assessment of non-interferometric measurements, especially when interferometric measurements do not exist as a reference. For example, we can estimate the maximum relative error for PMASW measurement at a frequency of 8.5 Hz with $\varepsilon < k_h/k_{\text{measure}} = 0.0023/0.05 = 4.6$ per cent. Besides, it is worth to point out a weak extension of the fundamental mode from 12 Hz to around 15 Hz in non-interferometric measurements (Figs 13a and b), particularly the ReMi measurement; the corresponding extension can also be observed on the MAPS measurement as light shadow energy (Fig. 13c) because of the relative stronger first higher

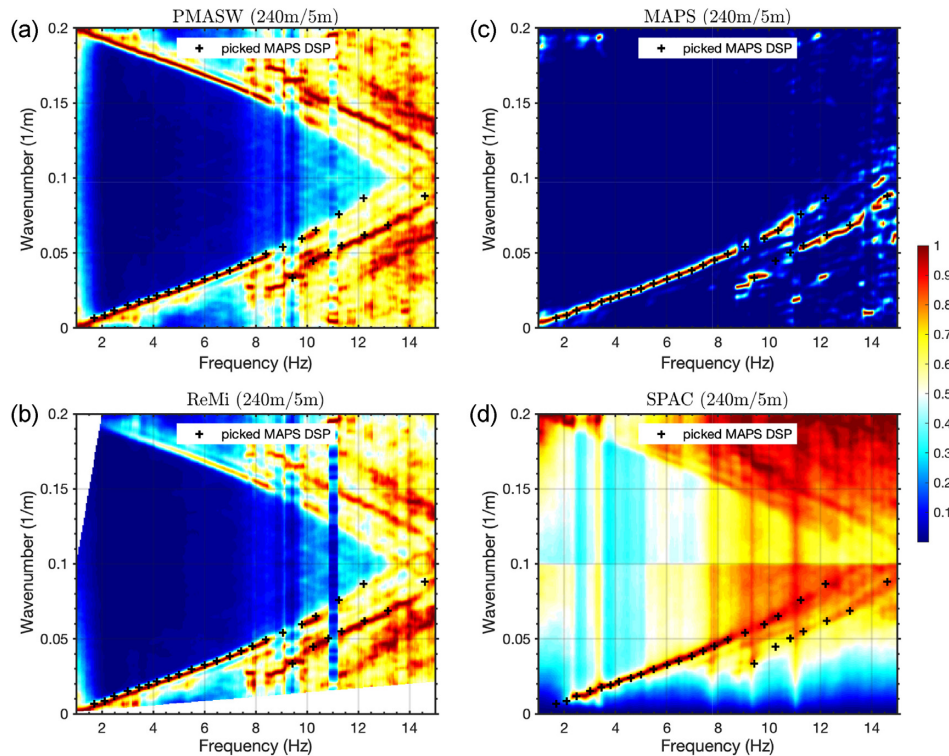


Figure 13. Measured dispersion spectra based on data set #2 with different passive surface wave methods, PMASW method (a), ReMi method (b), MAPS method (c) and SPAC method (d). The black crosses indicate the picked dispersion curve from MAPS measurement.

overtone occurring in the same frequency range. According to eq. (8), the true dispersion curve always stand at the top boundary of the apparent wavenumber energy for each individual dispersion spectral image (Fig. S3); with sufficient spectral stacking of the individual dispersion spectral images, non-interferometric methods have the potential advantage to highlight the lowest apparent dispersion energy boundary over interferometric methods which only use single-time dispersion measurement after temporal ensemble averaging/stacking. In this context, it is useful to use non-interferometric measurements as reference for interferometric measurement for dispersion curve picking, particularly at the high frequency band.

In order to verify the accuracy of the passive surface wave methods, we provide a comparison to the active surface wave measurement. We convert the active surface wave record (Fig. 14a) from the $x-t$ domain into the $f-v$ domain (Fig. 14b) using the high resolution linear radon transform (HLRT) developed by Luo *et al.* (2008). Fig. 14(c) displays the comparison between picked dispersion curves from the active surface wave measurement (MASW) and the passive surface wave measurement (MAPS). We observe great agreement between two fundamental mode curves and a similar trend for two first overtone curves. The consistency convinces us of the accuracy of the interferometric methods, as well as their advantages in lower frequency dispersion measurements relevant to deeper V_s estimation. For example, MAPS extends the lower frequency end of active measurement from 10 Hz to almost 1 Hz, and the maximum wavelength from 16 m to about 240 m.

3.3 Field data set #3

Fig. 15 shows the site map for field data set #3. A 240 m linear array recorded by a HX-DZ-02A 24-channel digital seismograph

was connected to 4.5 Hz vertical-component geophones, deployed along Dongting Avenue in Yueyang city. Continuous ambient seismic data (10-min records) were recorded with a 500 Hz sampling rate and a 10 m receiver spacing, and processed according to the previously described workflow and parameters. Fig. 16 presents a comparison between different passive surface wave methods, PMASW (Fig. 16a), ReMi (Fig. 16b), MAPS (Fig. 16c) and SPAC (Fig. 16d).

The goal of this comparison is to show how these passive surface wave methods behave with sparse spatial sampling. The symmetric spectra along the wavenumber direction (Figs 16a and b) is caused by the bidirectional velocity scanning scheme in non-interferometric surface wave methods (Cheng *et al.* 2018b). For example, the slant-stacking algorithm is scanning a reverse (backward) propagating surface wave train instead of the expected forward propagating one. Under the sparse spatial sampling configuration, these artefacts interfere with the true dispersion energy. We can observe the spectral energy around the crossed points becomes smeared for the non-interferometric measurement techniques; while MAPS method produces a clean dispersion image (Fig. 16c or Fig. 13c) because the direction of the scanning velocity has been defined as from virtual sources to virtual receivers. The existence of weak ‘crossed’ alias in SPAC measurement (Fig. 16d) is related with the periodicity and symmetry characteristic of Bessel function or Hankel function (Forbriger 2003; Cho *et al.* 2008; Xi 2021), which is beyond the scope of current work. The interested reader is referred to the works of Asten & Roberts (2006), Cho *et al.* (2006), Tada *et al.* (2007) and Cho *et al.* (2008) for discussions on the spatial aliasing of SPAC measurements due to the finite number of seismic sensors. Cheng *et al.* (2018b) first demonstrated this phenomenon as ‘crossed’ artefacts in $f-v$ domain and proposed an effective technique with data-selection to attenuate them. Xi *et al.* (2020) proposed to use the SVD-based Wiener filter to attenuate the

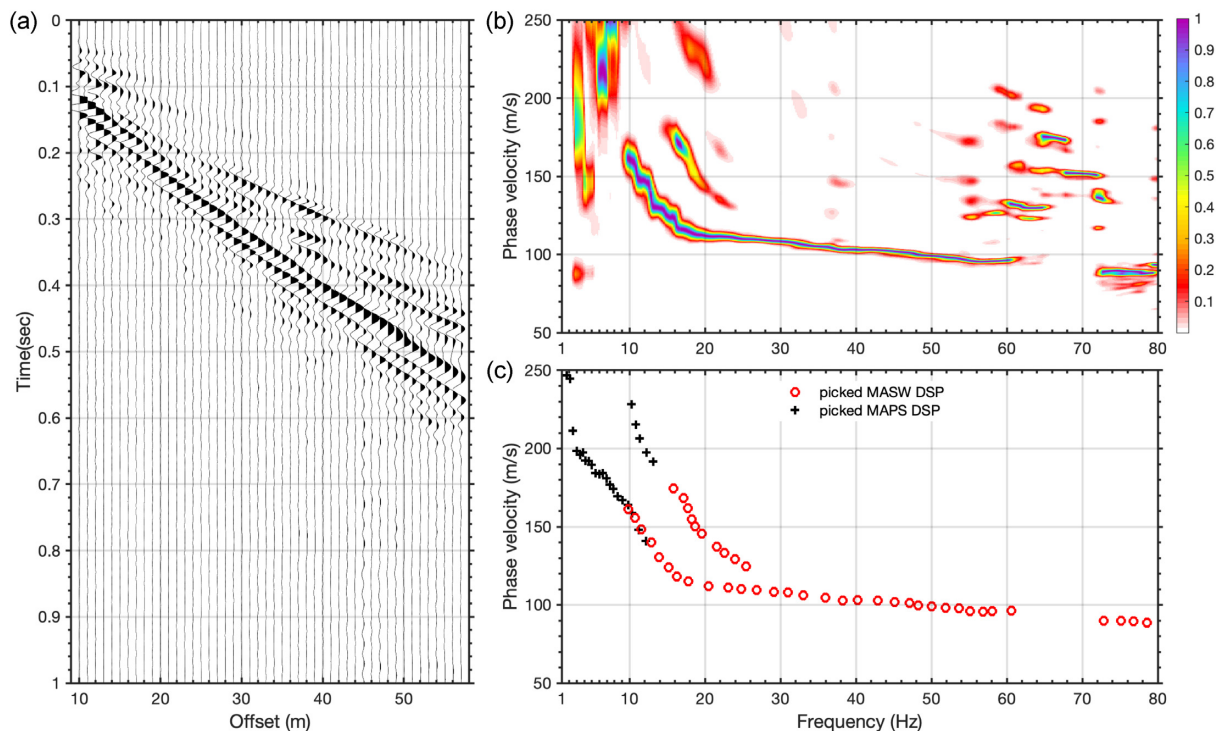


Figure 14. (a) Active-source surface wave shot gather (Z-component) along the receiver line. (b) Measured MASW dispersion spectra using HLRT method. (c) Comparison of the picked dispersion curves between MAPS measurement (black crosses) and MASW measurement (red dots).

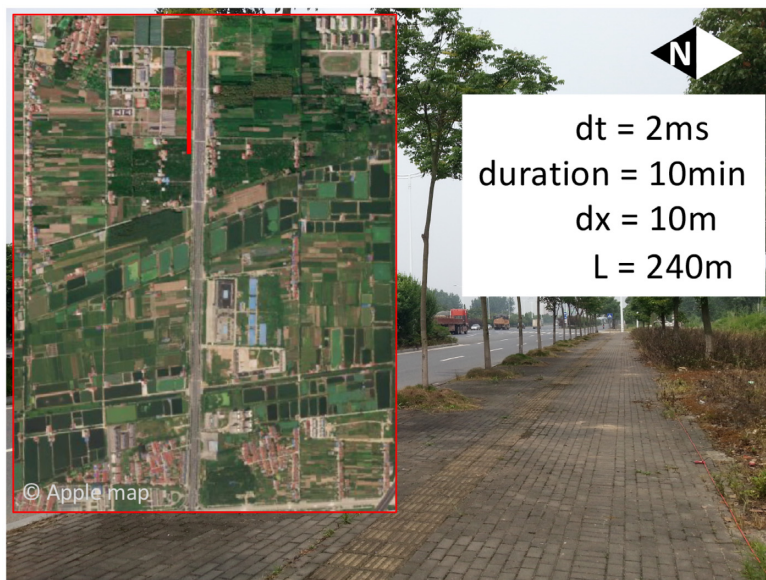


Figure 15. Site map of data set #3 with the receiver array along the Dongting Avenue in Yueyang city.

‘crossed’ artefacts. The more fundamental solution is to use a dense array; for example, we can get rid of the crossed spectral feature with a dense array, for example using a spatial interval of $dx = 5\text{m}$ and the corresponding Nyquist wavenumber limitation increasing to $k_{\text{Nyquist}} = 1/(2 \cdot dx) = 0.1\text{m}^{-1}$.

It is worth noticing the different aliasing features present on Fig. 11 ($dx = 1\text{m}$), Fig. 13 ($dx = 5\text{m}$) and Fig. 16 ($dx = 10\text{m}$) under different spatial intervals and array lengths. It indicates two key

parameters for the linear receiver array deployment: first, we need long array length to ensure imaging resolution, as well as propagation depth; second, we need fine spatial sampling intervals to ensure sufficient Nyquist wavenumber. Considering the deployment cost for cabled dense arrays, it might not be easy to fulfil both constraints. However, recent advances in nodal large-N deployments, as well as DAS acquisition, provide routes to solve these problems; DAS in particular allows for acquisition over tens of kilometres

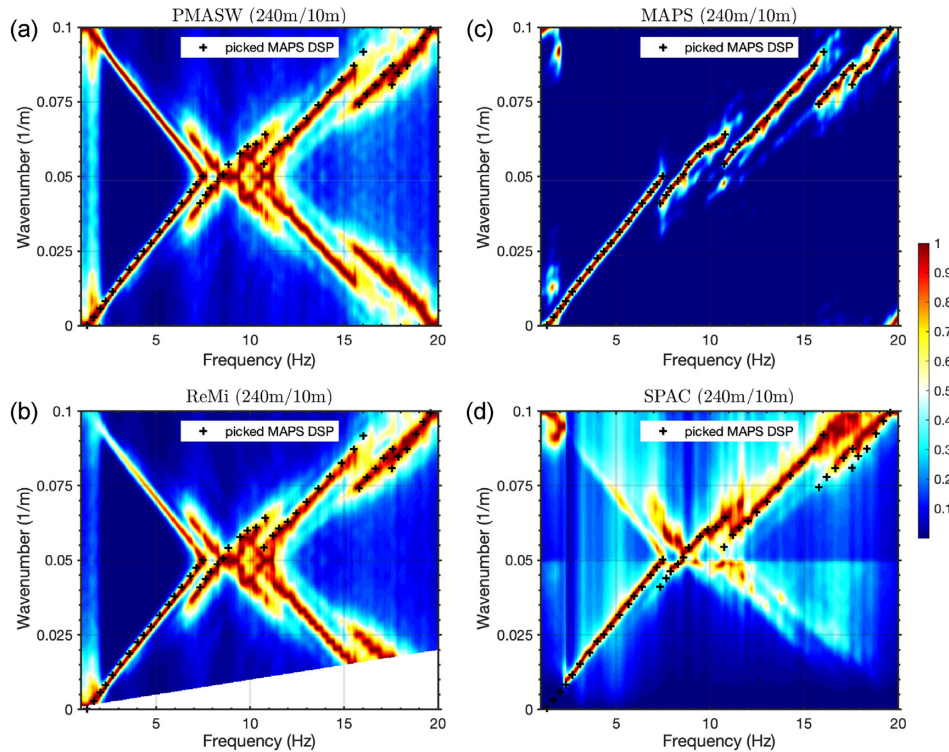


Figure 16. Measured dispersion spectra based on data set #3 with different passive surface wave methods, PMASW method (a), ReMi method (b), MAPS method (c) and SPAC method (d). The black crosses indicate the picked dispersion curve from MAPS measurement.

while providing spatial sampling in the metre range, thus enabling local surface wave analysis with high fidelity (Ajo-Franklin *et al.* 2019).

4 DISCUSSION

As the first comprehensive comparison work between non-interferometric and interferometric passive surface wave methods, we admit that further works are required to check the performances of these various techniques under the non-uniform noise source case. Whereas, two typical noise source distribution cases, random sources and linear sources, in this work are doubtlessly significant to illuminate the underlying physics of these various passive surface wave dispersion imaging techniques and lay a foundation for the further work. Besides, results in this work can also be extended to multicomponent passive surface waves (Xu *et al.* 2019, 2020).

The non-uniform noise source or the directional noise sources could produce biased cross-correlations, as well as biased dispersion measurements, particularly for linear receiver arrays. In order to attenuate the directional sources effect on dispersion measurements, Cheng *et al.* (2016) proposed to apply azimuthal adjustment to the slant-stacking algorithm. Our numerical derivations (eqs 12 and 17) exactly throw light on the ability of interferometric methods to reveal accurate dispersion measurements after azimuth adjustment. Liu *et al.* (2020) adapted a linear receiver array into a pseudo-linear array by adding two more off-line receivers to increase the array response to off-line signals, in order to address a similar problem with a linear array. On the other hand, data-selection is an effective tool for data quality control, and might be an alternative to mitigate influences from time segments in which non-uniform noise sources dominate. Studies have successfully used data-selection techniques on passive-source surface wave imaging for dispersion

spectra enhancement (e.g. Cheng *et al.* 2018b, 2019; Zhou *et al.* 2018; Pang *et al.* 2019; Xie *et al.* 2020a, b; Dangwal & Behm 2020).

5 CONCLUSIONS

We first derive numerical solutions for dispersion analysis of both non-interferometric and interferometric passive surface wave methods under two typical source distribution cases, random sources and linear sources. We prove the strength of interferometric methods for accurate dispersion imaging over the non-interferometric methods under two common noise source environments including a homogeneous source distribution (e.g. the quiet rural environment) and a dominant in-line source distribution (e.g. the urban traffic line environment). We present an approximate solution for non-interferometric methods when the required assumptions on the ideal noise source distribution fail, and provide a way to estimate the biases in non-interferometric measurements. We finally make comprehensive comparisons between different passive surface wave methods with three typical field examples, and conclude the following summaries.

1. In general, dispersion measurements of interferometric methods are cleaner and more accurate than those of non-interferometric methods.
2. Without considering the directional ambient source effects, non-interferometric methods are able to provide dispersion measurements with estimable biases using imaging resolution.
3. Compared to the MAPS method, the SPAC method has less sensitivity to the spectral peaks generated by higher order modes.

4. In terms of computing cost, the MAPS method is more efficient than the SPAC method without the costs of Bessel functions evaluation; the PMASW method is also more efficient than the ReMi method due to the frequency-domain slant-stacking.

ACKNOWLEDGMENTS

This study was supported by the National Natural Science Foundation of China under grant no. 41830103. We thank SISL crews, as well as AoCheng Tech crews, for the field-data acquisitions. Finally, we thank Editor Sidao Ni, E. Bozdog, Assistant Editor Fern Storey, Yong Zhou, Dylan Mikesell and other anonymous reviewers for their constructive and detailed comments that significantly improve our paper.

DATA AVAILABILITY

The real-world data underlying this paper will be shared on reasonable request to the corresponding author.

REFERENCES

- Ajo-Franklin, J.B. *et al.*, 2019. Distributed Acoustic Sensing using dark fiber for near-surface characterization and broadband seismic event detection, *Sci. Rep.*, **9**(1), 1328.
- Aki, K., 1957. Space and time spectra of stationary stochastic waves, with special reference to microtremors, *Bull. Earthq. Res. Inst.*, **35**, 415–456.
- Aki, K. & Richards, P.G., 2002. *Quantitative Seismology*, University Science Books.
- Ali, M.Y., Barkat, B., Berteussen, K.A. & Small, J., 2013. A low-frequency passive seismic array experiment over an onshore oil field in Abu Dhabi, United Arab Emirates, *Geophysics*, **78**(4), B159–B176.
- Asten, M. & Hayashi, K., 2018. Application of the spatial auto-correlation method for shear-wave velocity studies using ambient noise, *Surv. Geophys.*, **39**(4), 633–659.
- Asten, M. & Roberts, J., 1997. Geotechnical site characterization using surface waves in Earthquake Geotechnical Engineering, in *Proceedings of IS-Tokyo '95, The First International Conference on Earthquake Geotechnical Engineering*, Tokyo, 14–16 November, pp. 1333–1368.
- Asten, M. & Roberts, J., 2006. Analysis of ESG2006 blind-trial microtremor data using the MMSPAC method, in *Third International Symposium on the Effects of Surface Geology on Seismic Motion*, Grenoble, France, 30 August–1 September.
- Asten, M.W., 2006. On bias and noise in passive seismic data from finite circular array data processed using SPAC methods, *Geophysics*, **7**(6), 153–162.
- Asten, M.W., Dhu, T. & Lam, N., 2004. Optimised array design for microtremor array studies applied to site classification; comparison of results with septic logs, in *Proceedings of the 13th World Conference on Earthquake Engineering*, Vancouver, BC, Canada, 1–6 August.
- Asten, M.W. *et al.*, 2022. An assessment of uncertainties in VS profiles obtained from microtremor observations in the phased 2018 COSMOS blind trials, *J. Seismol.*, **26**, 757–780.
- Bajaj, K. & Anbazhagan, P., 2019. Comprehensive amplification estimation of the Indo Gangetic Basin deep soil sites in the seismically active area, *Soil Dyn. Earthq. Eng.*, **127**, doi:10.1016/j.soildyn.2019.105855.
- Bakulin, A. & Calvert, R., 2006. The virtual source method: Theory and case study, *Geophysics*, **71**(4), 139–150.
- Behm, M., Leahy, G.M. & Snieder, R., 2014. Retrieval of local surface wave velocities from traffic noise - an example from the La Barge basin (Wyoming), *Geophys. Prospect.*, **62**(2), 223–243.
- Behm, M., Cheng, F., Patterson, A. & Soreghan, G., 2019. Passive processing of active nodal seismic data: estimation of Vp/Vs ratios to characterize structure and hydrology of an alpine valley infill, *Solid Earth*, **10**, 1337–1354.
- Bensen, G.D., Ritzwoller, M.H., Barmin, M.P., Levshin, A.L., Lin, F., Moschetti, M.P., Shapiro, N.M. & Yang, Y., 2007. Processing seismic ambient noise data to obtain reliable broad-band surface wave dispersion measurements, *Geophys. J. Int.*, **169**, 1239–1260.
- Bergamo, P., Boiero, D. & Socco, L.V., 2012. Retrieving 2D structures from surface-wave data by means of space-varying spatial windowing, *Geophysics*, **77**(4), doi:10.1190/geo2012-0031.1.
- Birtill, J.W., Whiteway, F.E. & Penney, W.G., 1965. The application of phased arrays to the analysis of seismic body waves, *Phil. Trans. R. Soc. Lond., A.*, **258**(1091), 421–493.
- Boiero, D. & Socco, L.V., 2011. The meaning of surface wave dispersion curves in weakly laterally varying structures, *Near Surf. Geophys.*, **9**(6), 561–570.
- Campillo, M. & Paul, A., 2003. Long-range correlations in the diffuse seismic coda, *Science*, **299**(5606), 547–549.
- Castellanos, J.C., Clayton, R.W. & Juarez, A., 2020. Using a time-based sub-array method to extract and invert noise-derived body waves at Long Beach, California, *J. geophys. Res.*, **125**(5), doi:10.1029/2019JB018855.
- Chávez-García, F.J., Rodríguez, M. & Stephenson, W.R., 2006. Subsoil structure using SPAC measurements along a line, *Bull. seism. Soc. Am.*, **96**(2), 729–736.
- Cheng, F., Xia, J., Xu, Y., Xu, Z. & Pan, Y., 2015. A new passive seismic method based on seismic interferometry and multichannel analysis of surface waves, *J. appl. Geophys.*, **117**, 126–135.
- Cheng, F. *et al.*, 2016. Multi-channel analysis of passive surface waves based on cross-correlations, *Geophysics*, **81**(5), EN57–EN66.
- Cheng, F., Draganov, D., Xia, J., Behm, M. & Hu, Y., 2017. Deblurring directional-source effects for passive surface-wave surveys using multidimensional deconvolution, in *AGU Fall Meeting Abstracts*, abstract #S21C-0736.
- Cheng, F., Xia, J., Shen, C., Hu, Y., Xu, Z. & Mi, B., 2018a. Imposing active sources during high-frequency passive surface-wave measurement, *Engineering*, **4**(5), 685–693.
- Cheng, F., Xia, J., Xu, Z., Hu, Y. & Mi, B., 2018b. Frequency-wavenumber (FK)-based data selection in high-frequency passive surface wave survey, *Surv. Geophys.*, **39**, 661–682.
- Cheng, F., Xia, J., Behm, M., Hu, Y. & Pang, J., 2019. Automated data selection in the tau-p domain: application to passive surface wave imaging, *Surv. Geophys.*, **40**, 1211–1228.
- Cheng, F., Chi, B., Lindsey, N.J., Dawe, T.C. & Ajo-Franklin, J.B., 2021a. Utilizing distributed acoustic sensing and ocean bottom fiber optic cables for submarine structural characterization, *Sci. Rep.*, **11**(1), doi:10.1038/s41598-021-84845-y.
- Cheng, F., Xia, J., Ajo-Franklin, J.B., Behm, M., Zhou, C., Dai, T., Xi, C., Pang, J. & Zhou, C., 2021b. High-resolution ambient noise imaging of geothermal reservoir using 3C dense seismic nodal array and ultra-short observation, *J. geophys. Res.*, **2019**, doi:10.1029/2021JB021827.
- Cheng, F., Xia, J., Zhang, K., Zhou, C. & Ajo-Franklin, J.B., 2021c. Phase-weighted slant stacking for surface wave dispersion measurement, *Geophys. J. Int.*, **226**(1), 256–269.
- Cheng, F. *et al.*, 2022. Watching the cryosphere thaw: seismic monitoring of permafrost degradation using distributed acoustic sensing during a controlled heating experiment, *Geophys. Res. Lett.*, **49**(10), e2021GL097195, doi:10.1029/2021GL097195.
- Cho, I. & Iwata, T., 2021. Limits and benefits of the spatial autocorrelation microtremor array method due to the incoherent noise, with special reference to the analysis of long wavelength ranges, *J. geophys. Res.*, **126**(2), e2020JB019850, doi:10.1029/2020JB019850.
- Cho, I., Tada, T. & Shinozaki, Y., 2006. A generic formulation for microtremor exploration methods using three-component records from a circular array, *Geophys. J. Int.*, **165**(1), 236–258.
- Cho, I., Tada, T. & Shinozaki, Y., 2008. Assessing the applicability of the spatial autocorrelation method: a theoretical approach, *J. geophys. Res.*, **113**(B6), doi:10.1029/2007JB005245.
- Cornou, C., Ohrnberger, M., Boore, D.M., Kudo, K., Bard, P.-Y., Chaljub, E., Cotton, F. & Gueguen, P., 2006. Derivation of structural models from ambient vibration array recordings: results from an international blind

- test, in *Proceedings of the Third International Symposium on the Effects of Surface Geology on Seismic Motion*, NBT.
- Dangwal, D. & Behm, M., 2020. Meeting the stationary phase requirement for local ambient noise interferometry through polarization analysis, *AGU Fall Meeting 2020*, abstract #S020-0004, AGU.
- Darvasi, Y., 2021. Shear-wave velocity measurements and their uncertainties at six industrial sites, *Earthq. Spectra*, **37**(3), 2223–2246.
- Dorman, J. & Ewing, M., 1962. Numerical inversion of seismic surface wave dispersion data and crust-mantle structure in the New York-Pennsylvania area, *J. geophys. Res.*, **67**(13), 5227–5241.
- Dou, S. *et al.*, 2017. Distributed acoustic sensing for seismic monitoring of the near surface: a traffic-noise interferometry case study, *Sci. Rep.*, **7**(1), doi:10.1038/s41598-017-11986-4.
- Draganov, D., Campman, X., Thorbecke, J., Verdel, A. & Wapenaar, K., 2009. Reflection images from ambient seismic noise, *Geophysics*, **74**(5), A63–A67.
- Draganov, D., Ghose, R., Heller, K. & Ruigrok, E., 2013. Monitoring changes in velocity and Q using non-physical arrivals in seismic interferometry, *Geophys. J. Int.*, **192**(2), 699–709.
- Ekström, G., Abers, G.A. & Webb, S.C., 2009. Determination of surface-wave phase velocities across USArray from noise and Aki's spectral formulation, *Geophys. Res. Lett.*, **36**(18), doi:10.1029/2009GL039131.
- Fichtner, A., Tsai, V., Nakata, N. & Gualtieri, L., 2019. Theoretical foundations of noise interferometry, in *Seismic Ambient Noise*, pp. 109–143, eds Nakata, N., Gualtieri, L. & Fichtner, A., Cambridge Univ. Press.
- Fichtner, A., Bowden, D. & Ermer, L., 2020. Optimal processing for seismic noise correlations, *Geophys. J. Int.*, **223**(3), 1548–1564.
- Forbriger, T., 2003. Inversion of shallow-seismic wavefields: I. Wavefield transformation, *Geophys. J. Int.*, **153**(3), 719–734.
- Foti, S., Parolai, S., Albarello, D. & Picozzi, M., 2011. Application of surface-wave methods for seismic site characterization, *Surv. Geophys.*, **32**(6), 777–825.
- Foti, S., Lai, C.G., Rix, G.J. & Strobbia, C., 2014. *Surface Wave Methods for Near-Surface Site Characterization*, CRC Press.
- Foti, S. *et al.*, 2017. Guidelines for the good practice of surface wave analysis: a product of the InterPACIFIC project, *Bull. Earthq. Eng.*, **16**, 2367–2420.
- Fuchs, F. & Bokelmann, G., 2018. Equidistant spectral lines in train vibrations, *Seismol. Res. Lett.*, **89**(1), 56–66.
- Girard, A.J. & Shragge, J., 2019. Automated processing strategies for ambient seismic data, *Geophys. Prospect.*, **68**(1), 293–312.
- Halliday, D. & Curtis, A., 2008. Seismic interferometry, surface waves and source distribution, *Geophys. J. Int.*, **175**(3), 1067–1087.
- Haney, M.M., Mikesell, T.D., van Wijk, K. & Nakahara, H., 2012. Extension of the spatial autocorrelation (SPAC) method to mixed-component correlations of surface waves, *Geophys. J. Int.*, **191**(1), 189–206.
- Hayashi, K., Cakir, R. & Walsh, T.J., 2013. Using two-station microtremor array method to estimate shear-wave velocity profiles in Seattle and Olympia, Washington, in *Symposium on the Application of Geophysics to Engineering and Environmental Problems 2013*, pp. 442–451, Society of Exploration Geophysicists and Environment and Engineering.
- Hayashi, K., Craig, M., Kita, T. & Inazaki, T., 2015. CMP spatial autocorrelation analysis of multichannel passive surface-wave data, in *2015 SEG Annual Meeting. Society of Exploration Geophysicists*, pp. 2200–2204.
- Hayashi, K. *et al.*, 2016. Comparison of dispersion curves and velocity models obtained by active and passive surface wave methods, in *2016 SEG International Exposition and Annual Meeting*, Society of Exploration Geophysicists.
- Hayashi, K., Asten, M.W., Stephenson, W.J., Cornou, C., Hobiger, M., Pilz, M. & Yamanaka, H., 2022. Microtremor array method using spatial autocorrelation analysis of Rayleigh-wave data, *J. Seismol.*, **26**, 601–627.
- Hillers, G., Graham, N., Campillo, M., Kedar, S., Landés, M. & Shapiro, N., 2012. Global oceanic microseism sources as seen by seismic arrays and predicted by wave action models, *Geochem., Geophys., Geosyst.*, **13**(1), doi:10.1029/2011GC003875.
- Hu, S., Luo, S. & Yao, H., 2020. The frequency-Bessel spectrograms of multicomponent cross-correlation functions from seismic ambient noise, *J. geophys. Res.*, **125**(8), e2020JB019630, doi:10.1029/2020JB019630.
- Ikeda, T., Matsuoka, T., Tsuji, T. & Hayashi, K., 2012. Multimode inversion with amplitude response of surface waves in the spatial autocorrelation method, *Geophys. J. Int.*, **190**(1), 541–552.
- Johnson, D. & Dudgeon, D., 1993. *Array Signal Processing: Concepts and Techniques*, Prentice Hall, 533pp.
- Kedar, S., Longuet-Higgins, M., Webb, F., Graham, N., Clayton, R. & Jones, C., 2008. The origin of deep ocean microseisms in the North Atlantic Ocean, *Proc. R. Soc., A*, **464**(2091), 777–793.
- Kimman, W.P. & Trampert, J., 2010. Approximations in seismic interferometry and their effects on surface waves, *Geophys. J. Int.*, **182**(1), 461–476.
- Kita, T., Hayashi, K. & Bingol, H., 2011. The development of a 2-dimensional microtremor survey method based on SPAC method using sequential linear arrays, in *24th Symposium on the Application of Geophysics to Engineering and Environmental Problems 2011 (SAGEEP 2011)*, 10–14 April 2011, Charleston, SC, USA, European Association of Geoscientists & Engineers.
- Landés, M., Hubans, F., Shapiro, N.M., Paul, A. & Campillo, M., 2010. Origin of deep ocean microseisms by using teleseismic body waves, *J. geophys. Res.*, **115**(B5), doi:10.1029/2009JB006918.
- Lawrence, J.F. & Prieto, G.A., 2011. Attenuation tomography of the western United States from ambient seismic noise, *J. geophys. Res.*, **116**(B6), 1–11.
- Lawrence, J.F., Denolle, M., Seats, K.J. & Prieto, G.A., 2013. A numeric evaluation of attenuation from ambient noise correlation functions, *J. geophys. Res.*, **118**(12), 6134–6145.
- Le Feuvre, M., Joubert, A., Leparoux, D. & Côte, P., 2015. Passive multi-channel analysis of surface waves with cross-correlations and beamforming – application to a sea dike, *J. appl. Geophys.*, **114**, 36–51.
- Lehujeur, M., Vergne, J., Schmittbuhl, J., Zigone, D. & Le Chenadec, A., Team E., 2018. Reservoir imaging using ambient noise correlation from a dense seismic network, *J. geophys. Res.*, **123**(8), 6671–6686.
- Li, X. & Li, Q., 2018. Active-source Rayleigh wave dispersion by the AKI spectral formulation, *Appl. Geophys.*, **15**(2), 290–298.
- Lin, F., Moschetti, M.P. & Ritzwoller, M.H., 2008. Surface wave tomography of the western United States from ambient seismic noise: Rayleigh and Love wave phase velocity maps, *Geophys. J. Int.*, **173**(1), 281–298.
- Liu, Y., Xia, J., Cheng, F., Xi, C., Shen, C. & Zhou, C., 2020. Pseudo-linear-array analysis of passive surface waves based on beamforming, *Geophys. J. Int.*, **221**(1), 640–650.
- Liu, Y., Yue, Y., Luo, Y. & Li, Y., 2021. Effects of high-speed train traffic characteristics on seismic interferometry, *Geophys. J. Int.*, **227**(1), 16–32.
- Lobkis, O.I. & Weaver, R.L., 2001. On the emergence of the Green's function in the correlations of a diffuse field, *J. acoust. Soc. Am.*, **110**(6), 3011–3017.
- Louie, J., Pullammanappallil, S., Pancha, A., West, T. & Hellmer, W., 2011. Earthquake hazard class mapping by parcel in Las Vegas Valley, in *Structures Congress 2011*, pp. 1794–1805.
- Louie, J.N., 2001. Faster, better: shear-wave velocity to 100 meters depth from refraction microtremor arrays, *Bull. seism. Soc. Am.*, **91**(2), 347–364.
- Louie, J.N., Pancha, A. & Kissane, B., 2022. Guidelines and pitfalls of refraction microtremor surveys, *J. Seismol.*, **26**, 583–584.
- Luo, Y., Xia, J., Miller, R.D., Xu, Y., Liu, J. & Liu, Q., 2008. Rayleigh-wave dispersive energy imaging using a high-resolution linear radon transform, *Pure appl. Geophys.*, **165**(5), 903–922.
- Luo, Y., Xia, J., Xu, Y. & Zeng, C., 2011. Analysis of group-velocity dispersion of high-frequency Rayleigh waves for near-surface applications, *J. appl. Geophys.*, **74**(2–3), 157–165.
- Margaryan, S., Yokoi, T. & Hayashi, K., 2009. Experiments on the stability of the spatial autocorrelation method (SPAC) and linear array methods and on the imaginary part of the SPAC coefficients as an indicator of data quality, *Explor. Geophys.*, **40**(1), 121–131.
- Martins, J.E., Ruigrok, E., Draganov, D., Hooper, A., Hanssen, R., White, R. & Soosalu, H., 2019. Imaging Torfajökull's magmatic plumbing system with seismic interferometry and phase velocity surface wave tomography, *J. geophys. Res.*, **124**(3), 2920–2940.
- McMechan, G.A. & Yedlin, M.J., 1981. Analysis of dispersive waves by wave field transformation, *Geophysics*, **46**(6), 869–874.

- Morton, S.L., Ivanov, J., Peterie, S.L., Miller, R.D. & Livers-Douglas, A.J., 2021. Passive multichannel analysis of surface waves using 1D and 2D receiver arrays, *Geophysics*, **86**(6), EN63–EN75.
- Mulgaria, F. & Castellaro, S., 2013. A seismic passive imaging step beyond SPAC and REMI, *Geophysics*, **78**(5), KS63–KS72.
- Nakahara, H., 2006. A systematic study of theoretical relations between spatial correlation and Green's function in one-, two- and three-dimensional random scalar wavefields, *Geophys. J. Int.*, **167**(3), 1097–1105.
- Nakata, N., 2016. Near-surface S-wave velocities estimated from traffic-induced Love waves using seismic interferometry with double beam-forming, *Interpretation*, **4**(4), 23–31.
- Nakata, N., Snieder, R., Tsuji, T., Larner, K. & Matsuoka, T., 2011. Shear wave imaging from traffic noise using seismic interferometry by cross-coherence, *Geophysics*, **76**(6), SA97–SA106.
- Nakata, N., Snieder, R. & Behm, M., 2014. Body-wave interferometry using regional earthquakes with multidimensional deconvolution after wavefield decomposition at free surface, *Geophys. J. Int.*, **199**(2), 1125–1137.
- Nishida, K., 2011. Two-dimensional sensitivity kernels for cross-correlation functions of background surface waves, *Comptes Rend. Geosci.*, **343**(8–9), 584–590.
- O'Connell, D. R. H. & Turner, J.P., 2011. Interferometric multichannel analysis of surface waves (IMASW), *Bull. seism. Soc. Am.*, **101**(5), 2122–2141.
- Ogori, M., Nobata, A. & Wakamatsu, K., 2002. A comparison of ESAC and FK methods of estimating phase velocity using arbitrarily shaped microtremor arrays, *Bull. seism. Soc. Am.*, **92**(6), 2323–2332.
- Okada, H. & Suto, K., 2003. *The Microtremor Survey Method*, Society of Exploration Geophysicists.
- O'Neill, A. & Matsuoka, T., 2005. Dominant higher surface-wave modes and possible inversion pitfalls, *J. Environ. Eng. Geophys.*, **10**(2), 185–201.
- Paitz, P., Sager, K. & Fichtner, A., 2019. Rotation and strain ambient noise interferometry, *Geophys. J. Int.*, **216**(3), 1938–1952.
- Pancha, A., Anderson, J.G., Louie, J.N. & Pullammanappallil, S.K., 2008. Measurement of shallow shear wave velocities at a rock site using the ReMi technique, *Soil Dyn. Earthq. Eng.*, **28**(7), 522–535.
- Pancha, A., Pullammanappallil, S.K., West, L.T., Louie, J.N. & Hellmer, W.K., 2017. Large-scale earthquake-hazard class mapping by parcel in Las Vegas Valley, Nevada, *Bull. seism. Soc. Am.*, **107**(2), 741–749.
- Pang, J., Cheng, F., Shen, C., Dai, T., Ning, L. & Zhang, K., 2019. Automatic passive data selection in time domain for imaging near-surface surface waves, *J. appl. Geophys.*, **162**, 108–117.
- Park, C., Miller, R., Lafren, D., Neb, C., Ivanov, J., Bennett, B. & Huggins, R., 2004. Imaging dispersion curves of passive surface waves, in *SEG Technical Program Expanded Abstracts 2004*, pp. 1357–1360, Society of Exploration Geophysicists.
- Park, C.B. & Miller, R.D., 2008. Roadside passive multichannel analysis of surface waves (MASW), *J. Environ. Eng. Geophys.*, **13**(1), 1–11.
- Park, C.B., Miller, R.D., Xia, J. & Survey, K.G., 1998. Imaging dispersion curves of surface waves on multi-channel record, *SEG Expanded Abstracts*, **17**(1), 1377–1380.
- Planès, T., Obermann, A., Antunes, V. & Lupi, M., 2020. Ambient-noise tomography of the Greater Geneva Basin in a geothermal exploration context, *Geophys. J. Int.*, **220**(1), 370–383.
- Prieto, G.A., Lawrence, J.F. & Beroza, G.C., 2009. Anelastic Earth structure from the coherency of the ambient seismic field, *J. geophys. Res.*, **114**(7), 1–15.
- Pullammanappallil, S., Honjas, W. & Louie, J.N., 2003. Determination of 1-D shear wave velocities using the refraction microtremor method, in *Proceedings of the Third International Conference on the Application of Geophysical Methodologies and NDT to Transportation and Infrastructure*, Orlando, Florida.
- Quiros, D.A., Brown, L.D. & Kim, D., 2016. Seismic interferometry of railroad induced ground motions: body and surface wave imaging, *Geophys. Suppl. Mon. Not. R. astr. Soc.*, **205**(1), 301–313.
- Rosenblad, B.L. & Li, J., 2009. Comparative study of refraction microtremor (ReMi) and active source methods for developing low-frequency surface wave dispersion curves, *J. Environ. Eng. Geophys.*, **14**(3), 101–113.
- Ruigrok, E., Gibbons, S. & Wapenaar, K., 2017. Cross-correlation beam-forming, *J. Seismol.*, **21**(3), 495–508.
- Sánchez-Sesma, F.J. & Campillo, M., 2006. Retrieval of the Green's function from cross correlation: the canonical elastic problem, *Bull. seism. Soc. Am.*, **96**(3), 1182–1191.
- Schwab, F. & Knopoff, L., 1972. Fast surface wave and free mode computations, in *Methods in Computational Physics: Advances in Research and Applications*, Vol. **11**, pp. 87–180, Elsevier.
- Sergeant, A., Chmiel, M., Lindner, F., Walter, F., Roux, P., Chaput, J., Gimbert, F. & Mordret, A., 2020. On the Green's function emergence from interferometry of seismic wave fields generated in high-melt glaciers: implications for passive imaging and monitoring, *Cryosphere*, **14**(3), 1139–1171.
- Shapiro, N.M. & Campillo, M., 2004. Emergence of broadband Rayleigh waves from correlations of the ambient seismic noise, *Geophys. Res. Lett.*, **31**(7), doi:10.1029/2004GL019491.
- Shen, C., Wang, A., Wang, L., Xu, Z. & Cheng, F., 2015. Resolution equivalence of dispersion-imaging methods for noise-free high-frequency surface-wave data, *J. appl. Geophys.*, **122**, 167–171.
- Snieder, R., 2004. Extracting the Green's function from the correlation of coda waves: a derivation based on stationary phase, *Phys. Rev. E*, **69**(4), doi:10.1103/PhysRevE.69.046610.
- Stehly, L., Campillo, M. & Shapiro, N.M., 2006. A study of the seismic noise from its long-range correlation properties, *J. geophys. Res.*, **111**, 1–12.
- Stephenson, W.J., Louie, J.N., Pullammanappallil, S., Williams, R. & Odum, J.K., 2005. Blind shear-wave velocity comparison of ReMi and MASW results with boreholes to 200 m in Santa Clara Valley: implications for earthquake ground-motion assessment, *Bull. seism. Soc. Am.*, **95**(6), 2506–2516.
- Stephenson, W.J., Asten, M.W., Odum, J.K. & Frankel, A.D., 2019. Shear-wave velocity in the Seattle Basin to 2 km depth characterized with the krSPAC microtremor array method: insights for urban basin-scale imaging, *Seismol. Res. Lett.*, **90**(3), 1230–1242.
- Stirzaker, D., 2003. *Elementary Probability*, Cambridge Univ. Press.
- Strobbia, C. & Cassiani, G., 2011. Refraction microtremors: data analysis and diagnostics of key hypotheses, *Geophysics*, **76**(3), doi:10.1190/1.3560246.
- Strobbia, C., Boaga, J. & Cassiani, G., 2015. Double-array refraction microtremors, *J. appl. Geophys.*, **121**, 31–41.
- Tada, T., Cho, I. & Shinozaki, Y., 2007. Beyond the SPAC method: exploiting the wealth of circular-array methods for microtremor exploration, *Bull. seism. Soc. Am.*, **97**(6), 2080–2095.
- Thelen, W.A. et al., 2006. A transect of 200 shallow shear-velocity profiles across the Los Angeles basin, *Bull. seism. Soc. Am.*, **96**(3), 1055–1067.
- Thorson, J.R. & Claerbout, J.F., 1985. Velocity-stack and slant-stack stochastic inversion, *Geophysics*, **50**(12), 2727–2741.
- Tromp, J. & Dahlen, F.A., 1993. Variational principles for surface wave propagation on a laterally heterogeneous earth-III. Potential representation, *Geophys. J. Int.*, **112**(2), 195–209.
- Tromp, J., Luo, Y., Hanasoge, S. & Peter, D., 2010. Noise cross-correlation sensitivity kernels, *Geophys. J. Int.*, **183**(2), 791–819.
- Tsai, V.C. & Moschetti, M.P., 2010. An explicit relationship between time-domain noise correlation and spatial autocorrelation (SPAC) results, *Geophys. J. Int.*, **182**(1), 454–460.
- Ushakov, N., 2001. *Density of a Probability Distribution*, Springer.
- Wang, J., Wu, G. & Chen, X., 2019. Frequency-Bessel transform method for effective imaging of higher-mode Rayleigh dispersion curves from ambient seismic noise data, *J. geophys. Res.*, **124**(4), 3708–3723.
- Wapenaar, K., 2004. Retrieving the elastodynamic Green's function of an arbitrary inhomogeneous medium by cross correlation, *Phys. Rev. Lett.*, **93**(25), doi:10.1103/PhysRevLett.93.254301.
- Wapenaar, K. & Ruigrok, E., 2011. Improved surface-wave retrieval from ambient seismic noise by multi-dimensional deconvolution, *Geophys. Res. Lett.*, **38**(January), 1–5.
- Wapenaar, K., van der Neut, J., Ruigrok, E. & van der Neut, J., 2008. Passive seismic interferometry by multidimensional deconvolution, *Geophysics*, **73**(NO.6), A51–A56.

- Weemstra, C., Westra, W., Snieder, R. & Boschi, L., 2014. On estimating attenuation from the amplitude of the spectrally whitened ambient seismic field, *Geophys. J. Int.*, **197**(3), 1770–1788.
- Wu, D., Sun, C. & Lin, M., 2017. Active seismic surface wave dispersion imaging method based on cross-correlation and phase-shifting (in Chinese), *Prog. Geophys.*, **32**(4), 533.
- Xi, C., 2021. Causes and attenuation of “rossed” artifacts in passive surface wave dispersion analysis, *PhD thesis*, Zhejiang University, Zhejiang, China.
- Xi, C., Mi, B., Dai, T., Liu, Y. & Ning, L., 2020. Spurious signals attenuation using SVD-based Wiener filter for near-surface ambient noise surface wave imaging, *J. appl. Geophys.*, **183**, doi:10.1016/j.jappgeo.2020.104220.
- Xi, C., Xia, J., Mi, B., Dai, T., Liu, Y. & Ning, L., 2021. Modified frequency–Bessel transform method for dispersion imaging of Rayleigh waves from ambient seismic noise, *Geophys. J. Int.*, **225**(2), 1271–1280.
- Xia, J., Miller, R.D. & Park, C.B., 1999. Estimation of near-surface shear-wave velocity by inversion of Rayleigh waves, *Geophysics*, **64**(3), 691–700.
- Xia, J., Xu, Y. & Miller, R.D., 2007. Generating an image of dispersive energy by frequency decomposition and slant stacking, *Pure appl. Geophys.*, **164**(5), 941–956.
- Xia, J. *et al.*, 2020a. Segment selection of cultural noise recordings in urban environment to improve quality of surface-wave image, in *Proceedings of the Fifth International Conference on Engineering Geophysics (ICEG)*, 21–24 October 2019, Al Ain, UAE, pp. 6–10, Society of Exploration Geophysicists.
- Xie, J., Yang, Y. & Luo, Y., 2020b. Improving cross-correlations of ambient noise using an rms-ratio selection stacking method, *Geophys. J. Int.*, **222**(2), 989–1002.
- Xu, Y., Zhang, B., Luo, Y. & Xia, J., 2013. Surface-wave observations after integrating active and passive source data, *Leading Edge*, **32**(6), 634–637.
- Xu, Z., Dylan Mikesell, T., Xia, J. & Cheng, F., 2017. A comprehensive comparison between the refraction microtremor and seismic interferometry methods for phase-velocity estimation, *Geophysics*, **82**(6), EN99–EN108.
- Xu, Z., Mikesell, T.D., Gribler, G. & Mordret, A., 2019. Rayleigh-wave multi-component cross-correlation-based source strength distribution inversion. Part 1: Theory and numerical examples, *Geophys. J. Int.*, **218**(3), 1761–1780.
- Xu, Z., Mikesell, T.D., Umlauf, J. & Gribler, G., 2020. Rayleigh-wave multi-component cross-correlation-based source strength distribution inversions. Part 2: a workflow for field seismic data, *Geophys. J. Int.*, **222**(3), 2084–2101.
- Yan, Y., Sun, C., Lin, T., Wang, J., Yang, J. & Wu, D., 2021. Surface-wave simulation for the continuously moving seismic sources, *Seismol. Res. Lett.*, **92**(4), 2429–2440.
- Yang, Y., Ritzwoller, M.H., Levshin, A.L. & Shapiro, N.M., 2007. Ambient noise Rayleigh wave tomography across Europe, *Geophys. J. Int.*, **168**(1), 259–274.
- Yao, H. & van der Hilst, R.D., 2009. Analysis of ambient noise energy distribution and phase velocity bias in ambient noise tomography, with application to SE Tibet, *Geophys. J. Int.*, **179**(2), 1113–1132.
- Zhan, Z., 2020. Distributed acoustic sensing turns fiber-optic cables into sensitive seismic antennas, *Seismol. Res. Lett.*, **91**(1), 1–15.
- Zhou, C., Xi, C., Pang, J. & Liu, Y., 2018. Ambient noise data selection based on the asymmetry of cross-correlation functions for near surface applications, *J. appl. Geophys.*, **159**, 803–813.

SUPPORTING INFORMATION

Supplementary data are available at *GJI* online.

Figure S1. Comparisons of non-interferometric and interferometric methods on uniform source distribution models, including the homogeneous distribution case (left-hand panel) and the random distribution case (right-hand panel). (a) Source–receiver configuration with the homogeneous source distribution (the colour coded by the random source impulse time) and the linear receiver array. Panels (b) and (c): Dispersion spectra measured by non-interferometric method (PMASW) and interferometric method (MAPS). (d) Source–receiver configuration with the random source distribution (the colour coded by the random source impulse time) and the linear receiver array. Panels (e) and (f): Dispersion spectra measured by non-interferometric method (PMASW) and interferometric method (MAPS). (g) Zoomed-in view of the highlighted window in (e). The black dashed lines show the theoretical dispersion curves. Note that we set a uniform source emitting time ($t_0 = 0$) in a to fulfil the ideal imaging environment.

Figure S2. Probability density function (PDF) of cosine of a random θ . on $(0, 2\pi)$. The grey bars show the histogram of $\cos\theta$, which has been normalized to estimate PDF; the red curve displays the theoretical PDF distribution of $\cos\theta$. 1000 variables of θ are randomly sampled between 0 and 2π .

Figure S3. PMASW dispersion measurements of a series of individual noise segments before stacking with source–receiver configuration presented on Fig. 7(d). No power spectra gain is applied here. The synthetic dispersion curve acts as a fixed boundary between the apparent wavenumber energy and weak random noise energy.

Figure S4. Biases of dispersion curve picking for non-interferometric dispersion measurements. The black dashed line shows the normalized dispersion energy envelope at 17 Hz, which is extracted from the dispersion spectra in Fig. 8(b); the blue dotted line shows the absolute gradient of the dispersion envelope curve; the red vertical line indicates the theoretical wavenumber value at 17 Hz. The black square at the bottom denotes the picked wavenumber value at the dispersion energy peak; the blue square denotes the picked wavenumber value at the steepest gradient of the dispersion energy envelope; the red square denotes the true theoretical wavenumber value. Both picking methods, using the energy peak and using the steepest gradient, introduce biases into measured phase velocities.

Please note: Oxford University Press is not responsible for the content or functionality of any supporting materials supplied by the authors. Any queries (other than missing material) should be directed to the corresponding author for the paper.